INFLUENCE OF LOADING WIDTH ON WEB COMPRESSION BUCKLING OF STEEL BEAMS

by

Jacob Witte

A Thesis

Submitted to the Faculty of Purdue University

In Partial Fulfillment of the Requirements for the degree of

Master of Science in Civil Engineering

Lyles School of Civil Engineering

West Lafayette, Indiana

December 2019

THE PURDUE UNIVERSITY GRADUATE SCHOOL
STATEMENT OF COMMITTEE APPROVAL

Dr. Amit H. Varma, Chair
School of Civil Engineering

Dr. Robert J. Connor
School of Civil Engineering

Dr. Mark D. Bowman
School of Civil Engineering

Approved by:
Dr. Dulcy M. Abraham

Dedicated to my friends and family who pushed me to succeed.

ACKNOWLEDGMENTS

First, I would like to thank Professor Amit Varma of Purdue University and Professor Kadir Sener of Auburn University for their help throughout my graduate studies at Purdue University. Both of you have been great teachers and mentors during my time here and I am extremely thankful for the opportunity to work with you. I would like to thank my parents and family for always supporting me in my studies and encouraging me to push myself. I would also like to thank Research Engineer Tom Bradt for all his assistance in the lab conducting experiments, preparing specimens, operating equipment, and everything else I needed to complete this research. Dr. Cem Korkmaz was also crucial with his assistance in developing the finite element models used in the parametric study and is deserving of recognition.

Thank you to Professors Mark Bowman and Robert Connor for serving on my Examining Committee, and their assistance in drafting this thesis. I would like to thank my fellow graduate students Morgan Broberg, Will Rich, Soheil Shafaei, Ata Taghipour, and the other graduate students at the Bowen Lab for their friendship and support.

This research was conducted at Purdue University's Bowen Laboratory for Large Scale Civil Engineering Research, and steel specimens were donated by Steel Dynamics, Inc. I would like to thank everyone at the lab, all the support staff and the people I have been lucky enough to call my coworkers for the past 18 months.

TABLE OF CONTENTS

LIST OF TABLES

LIST OF FIGURES

ABSTRACT

This paper presents an experimental and numerical study of the behavior of steel wide flange sections subjected to loads causing compression buckling in the web. This research includes experimental investigation of the effects of load width and duration on web compression buckling. This data is then used to calibrate numerical models. Experimental investigations were conducted on specimens with load widths of approximately 2.5, 1.75, and 1.5 times their section depth. Loads sustained on the specimens had a magnitude of about 85% of the expected buckling strength to investigate creep effects near failure. Results of these experiments were used to calibrate numerical models for a parametric study.

The numerical parametric study examined 60 specimens of 4 wide flange sections, investigating the effects of loaded width and angle of load application on web compression buckling. The numerical models accounted for initial imperfections in the specimens by applying imperfections with a magnitude of $0.13*t_w$ to the first mode shape obtained from a linear perturbation analysis. This value of imperfection was chosen because it is the average imperfection measured in the experimental specimens and is likely a good representation of a typical wide flange section.

A prediction method is provided based on the data obtained by the numerical parametric study. This prediction method is provided derived from rectangular plate buckling and considers the cases where the width of the concentrated load is not small compared to the section depth and when the applied load is not orthogonal to the specimen. The current AISC 360-16 provisions do not directly address the influence of load width in the calculation of web compression buckling strength and refer to the design of compression members when the loaded width is greater than or equal to the section depth. The AISC approach was evaluated and is a conservative approach to design.

1. INTRODUCTION

1.1 Background Information and Purpose

In the design of steel members, buckling in the members and their components should be considered. Steel is a very strong material relative to its weight, so designers want to use thinner, lighter components in design. Wide flanged shapes are no exception. Thinner flanges and webs make the sections lighter and potentially more efficient but can leave the section susceptible to local buckling issues. Figure 1.1 displays the dimensions of a wide flange section and the primary web compression buckling mode.

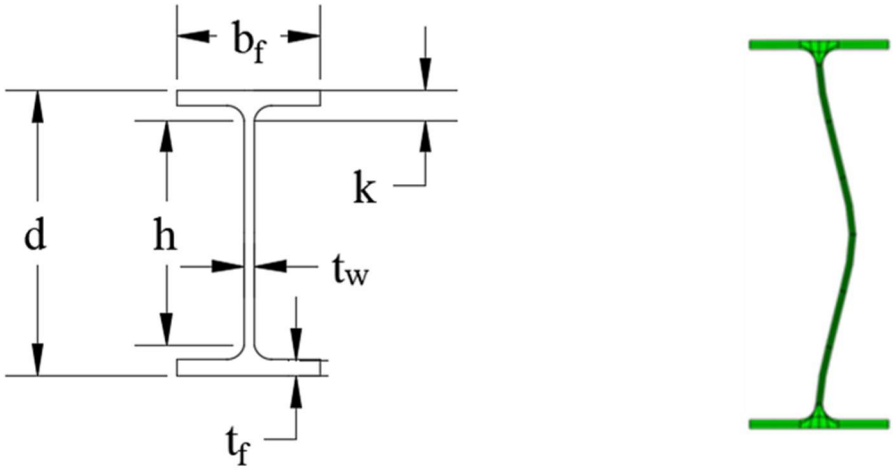

Figure 1.1: (a) W-Shape Labeling Diagram and (b) Web Compression Buckling Mode Shape

Figure 1.1(a) defines the dimensions of the wide flange section including the section depth, *d*, unstiffened height of the web, *h*, and thickness of the web, t_w, amongst others These are the dimensions primarily used throughout this paper. Figure 1.1(b) shows the expected web compression buckling mode shape. This mode shape assumes the flanges are detailed to prevent rotation.

The most common construction details that can lead to web compression buckling are moment connections between a beam and a column where beams come together on both sides of the column. An example of this detail is shown in Figure 1.2.

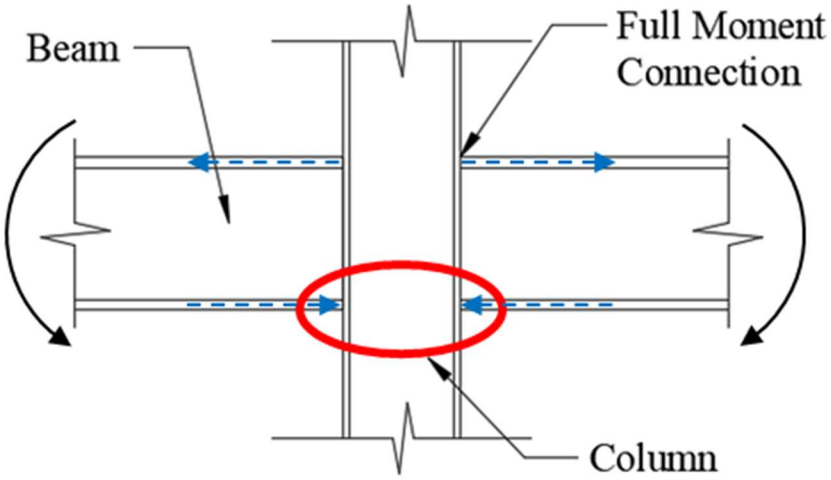

Figure 1.2: Typical Beam to Column Moment Connection

As shown in Figure 1.2, the compression flanges in the beams come together and try to pinch the web of the column together. The black arrows show the negative moment applied to this detail from typical gravity loads and the blue arrows represent the resultant force couples applied to the column. The region in the column susceptible to web compression buckling is where the compression forces meet the column web, marked by the red ellipse.

AISC Specification Section J10 discusses steel sections subjected to these types of concentrated loads. The AISC provisions regarding web sidesway buckling and web local crippling both account for the load width, or bearing length, in the available strength calculation. Web compression buckling however does not include such measures. The provided strength equation for web compression buckling (Equation J10-8) is reproduced below as Equation 1.1.

$$R_n = \frac{24 * t_w^3 \sqrt{E * f_y}}{h} * Q_f \tag{1.1}$$

The equation accounts for web thickness, t_w, modulus of elasticity, E, height of the web, h, and yield stress, f_y. The equation does make any consideration of loaded width. This equation was developed for use in the design of connections like the one shown in Figure 1.2. The loaded width of the webs in this detail is quite small (the width of the compression flange), so the strength equation neglects its contribution. However, a slight change in detailing, like the connection shown in Figure 1.3, increases the web compression buckling region and thus should have a higher strength.

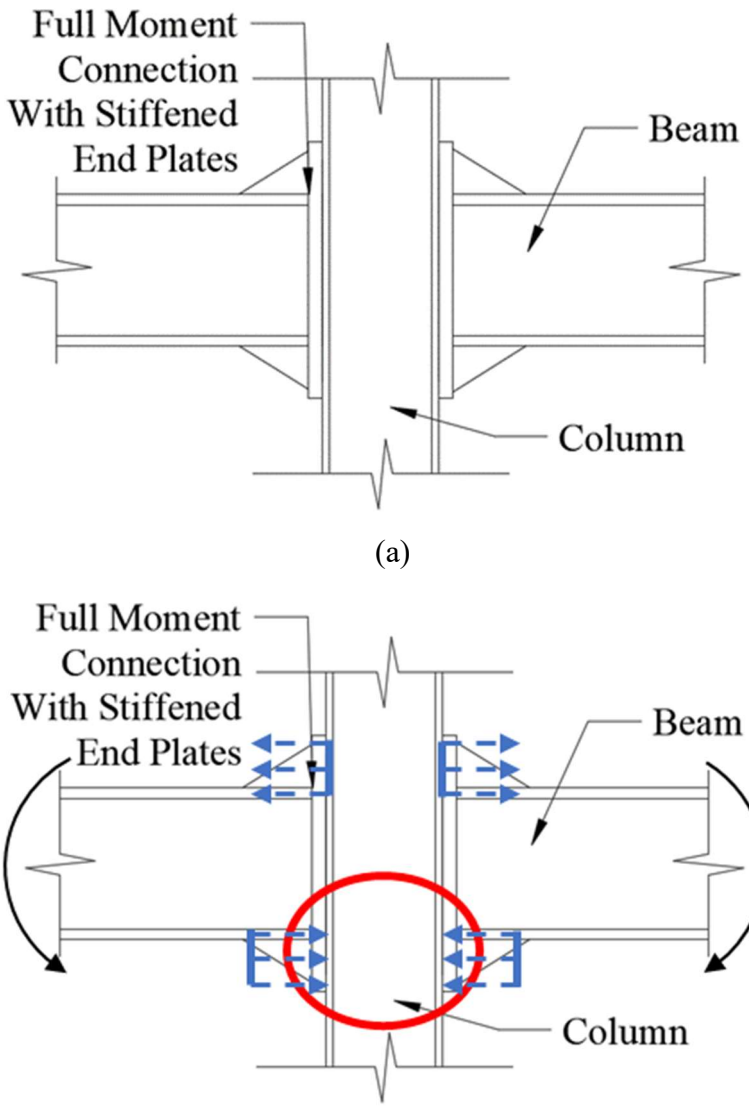

Figure 1.3: (a) Beam to Column Moment Connection with Stiffened End Plates and (b) Resultant Forces Causing Web Compression Buckling

This connection in Figure 1.3 uses stiffened end plates on the beams to transfer the moments from the beams to the column. This connection type is a common choice when the beam flange to column flange weld is difficult to design or fabricate. The addition of the stiffener plates on the beams greatly increases the area of column web subjected to the compression forces, and applies distributed compression loads to the column web rather than point loads from the flanges. This detail increases the loaded width on the column web, and the web compression buckling strength of the new compression region should be larger than the one in Figure 1.2.

Web compression buckling is not only an issue when designing beam to column moment connections, but also may occur in other common details like those shown in Figure 1.4 and Figure 1.5 below.

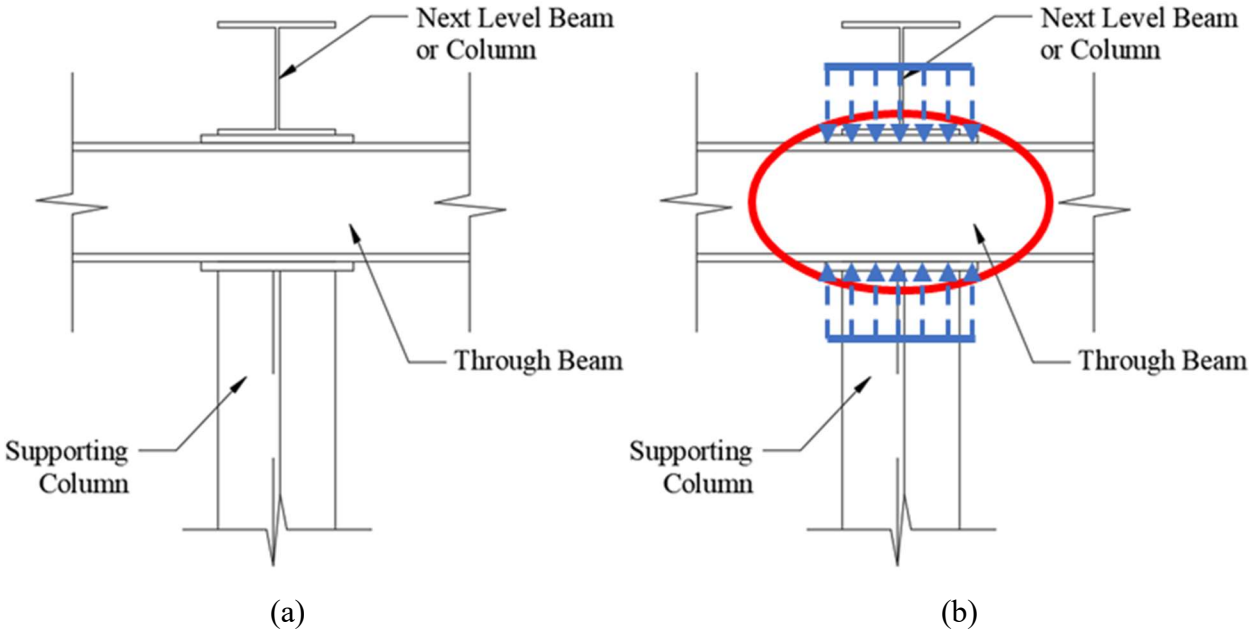

Figure 1.4: (a) Typical Through Beam Connection Over Supporting Column and (b) Resultant Forces Causing Web Compression Buckling

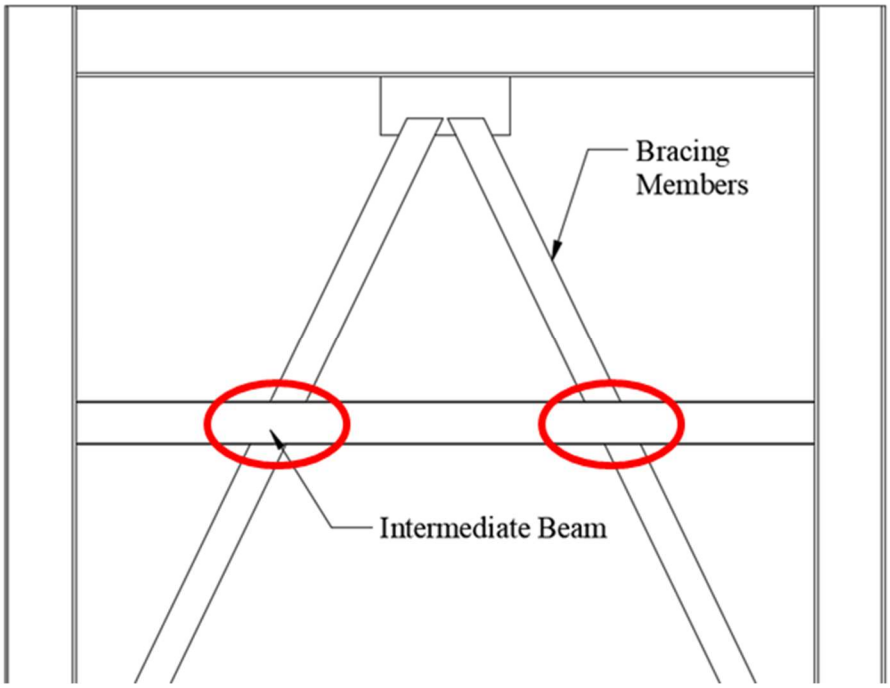

Figure 1.5: Typical A-Frame with Intermediate Beam

Figure 1.4 and Figure 1.5 provide examples where web compression buckling can occur over a large section of the web in situations unrelated to moment connections. Figure 1.4(a) shows a beam running over the end of a column but supporting another beam directly above it. Figure 1.4(b) shows how, under gravity loads, this detail could cause the area of the web marked by the red ellipse to experience web compression buckling. The loaded width in this scenario is the width of the baseplates used in the connection. This width engages more of the beam web to resist the compressive force and should be considered in design. Figure 1.5 shows an A-Frame with an intermediate beam. The diagonal bracing members are attached to each flange of the intermediate beam subjecting the region in the red ellipse to high compressive forces, which could cause web compression buckling. In both cases, the flanges would be restrained from rotating, so the earlier assumption against considering flange rotation appears valid.

In addition to compressive forces over a significant length, the connection marked in Figure 1.5 also features compression applied at an angle that is not orthogonal to the axis of the intermediate beam. The effect of this angle of application is unknown and should be considered.

It should be noted that the flow of forces shown in the figures in this section are not precisely representative of the actual flow of forces in the structures. The figures are provided as a visual aid to provide background into cases where web compression buckling can occur, not to be used as a design aid.

1.2 Research Objectives and Scope

The primary objective of this paper is to investigate the effect that loaded width, abbreviated w, has on the limit state of web compression buckling. Additionally, the effect of changing the angle of application away from orthogonal, abbreviated θ, will also be explored. These effects are easiest to examine through a parametric study of numerical finite element models. Experimental tests will be conducted to provide benchmarking data for these numerical models.

This paper also explores the effects of sustained loads on the limit state of web compression buckling through experimental procedures. Most research on the ambient temperature creep effects of steel come from uniaxial tension tests such as those conducted by Brnic (2010). The tests show that creep deformations in steel are negligible at room temperatures even near yielding. This paper examines whether this conclusion holds true in the case of compression buckling where the sustained load is near the expected buckling load.

Chapter 2 presents a literature review on the topic of web compression buckling. Additionally, classical solutions of plate buckling were included in the literature review.

Chapter 3 presents the experimental testing procedure. This includes the setups built, instrumentation used, loading protocol, etc. The specific materials used, fabrication, and measurements taken are also discussed.

Chapter 4 discusses the numerical modeling procedure used to replicate the experimental tests. These numerical models were not used in the parametric study, but instead used to provide insight into the effectiveness of the experimental procedures in real time.

Chapter 5 presents the experimental results from the procedures described in Chapter 3. The experimental results from Chapter 3 are compared with the numerical results obtained from the processes in Chapter 4. This chapter also contains discussion on what kinds of conclusions can be drawn from the experimental results alone.

Chapter 6 describes the parametric modeling procedure and results. The ABAQUS model selection and generation processes are discussed. Conclusions and insights drawn from the experimental testing are applied to the parametric study.

Chapter 7 presents a new prediction method for calculating the web compression buckling strength where the loaded width is a significant dimension. The theoretical background and classical solutions that lead to this development are also discussed here. This new prediction method is compared with the current design recommendations provided by AISC.

Chapter 8 summarizes the conclusions drawn from this paper. Conclusions and recommendations discussed in previous chapters are summarized again here.

2. LITERATURE REVIEW

2.1 Web Compression Buckling

2.1.1 Web compression buckling considering loaded width

One of the most recent papers published on this topic was authored by Dr. Fatmir Menkulasi and Dr. Nahid Farzana (Menkulasi & Farzana 2019). This paper is a journal article continuation of a conference proceeding from 2016 (Menkulasi et al 2016). This paper conducted numerical research on what the authors described as "opposite patch loading" at interior and end locations shown in Figure 2.1.

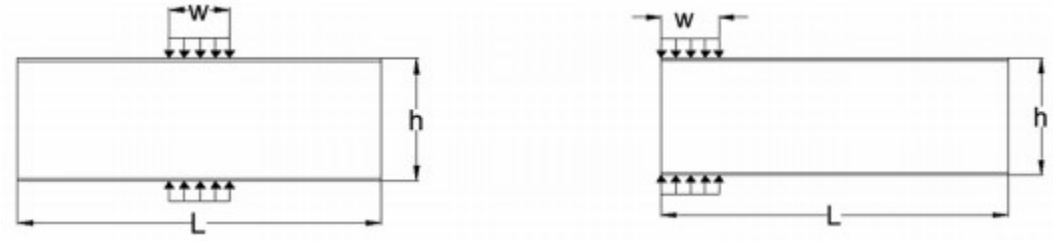

Figure 2.1: Opposite Patch Loading from Menkulasi et al 2016

The numerical parametric study featured a variety of I-shaped members varying from depths of 200 millimeters (mm) to 760mm for beam sections and 250mm to 360mm for column sections. The loaded widths, *w*, varied as a function of the depth, from $1/20^{th}$ of the depth (to simulate beam flanges like in Figure 1.2) to a width equal to the depth (to simulate Figure 1.4). The effect of strain hardening on web compression buckling was also investigated in this study and was found to have minimal impact on the performance of the specimen. The models were created using the ABAQUS finite element software. The wide flange members were modeled using shell elements to represent the flanges and web. The unstiffened height on the web, *h*, was defined as the distance between the centroids of the flanges. The flanges were restrained from rotation, like the assumption made in Chapter 1. The authors used a modified Riks analysis technique where the critical elastic buckling load is obtained from a linear perturbation eigenvalue analysis, then initial imperfections are applied to the first resulting mode shape for use in the static Riks analysis. A similar numerical simulation approach will be used in this paper. The numerical

data was benchmarked to a previously available set of experimental data found in papers by Chen and Oppenheim (1971, 1973) and Chen and Newlin (1970, 1974).

The authors then developed prediction methods for web compression buckling from their data. The prediction method begins by predicting the elastic buckling load by considering existing solutions for infinitely wide plates subjected to discrete patch loading. A method for predicting the squash load, or yield load, is then proposed. With two analogous values of critical elastic load and yield load, a method similar to the AISC 360 Chapter E column curve is proposed for predicting the available resistance.

The results from this parametric study are used as supplemental data points in this paper, marked as "Menkulasi FEM Results" in the appropriate figures. In calculations involving this set of data, the value of h is defined as the distance between the centroids of the two flanges.

2.1.2 Web compression buckling considering point loads

AISC 360-16 Section J10 provides an available strength equation for the limit state of web compression buckling. This equation does not account for load width as a parameter, so it would predict the same strength whether the total force is applied at a point or spread out over a significant width. In the Commentary, AISC 360 discusses how the provided equation is meant for calculating the web compression buckling in columns in a beam to column moment connection like the one shown in Figure 1.2. The Commentary also suggests that when the width of the applied load is larger than the depth of the section, the provisions from Chapter E should be used instead. There is no reference provided for this suggestion, and its validity is evaluated later in this paper.

2.2 Elastic Plate Buckling

2.2.1 Rectangular plate buckling

Timoshenko and Gere's book *Theory of Elastic Stability* (1961) provides many classical solutions to plate buckling problems. The equations for elastic buckling load are derived by examining the strain energy associated with buckling and considering a sinusoidal shape function in both directions. This calculation also assumes load is applied in only one direction and the plate is isotropic.

After many pages of calculus and algebra, Timoshenko arrives at Equation 2.1 for critical elastic buckling load, P_{cr}, for a rectangular plate simply supported on all sides with dimensions *a* and *b* where dimension *b* is perpendicular to the direction of loading.

$$P_{cr} = k\frac{\pi^2 D}{b} \tag{2.1}$$

Where *D* is the flexural rigidity of the plate, defined as:

$$D = \frac{Eh^3}{12(1-\nu^2)} \tag{2.2}$$

The variable *h* in this case represents the thickness of the plate and *E* and *v* are the modulus of elasticity and Poisson's ratio respectively. The plate buckling coefficient *k* is a function of the aspect ratio of the plate, *a/b*, and the number of buckled half-sine waves in the plate. The buckled shape changes from 1 to 2 buckled sine waves in the direction of *a*, is when the aspect ratio, *a/b*, reached $\sqrt{2}$. Timoshenko also derived that as *a/b* increased towards infinity, the value of *k* approached 4. Therefore, the elastic buckling coefficient of an infinitely long rectangular plate is 4, and plates could be assumed as "infinitely long" for the sake of analysis when *a/b* is greater than or equal to 2.

For the case of web compression buckling, not often are these criteria met, nor is *a/b* greater than $\sqrt{2}$. Therefore only 1 buckled sine wave is assumed when the web of an I-shaped member buckles in compression. With this assumption, Timoshenko's function for *k* becomes:

$$k = \left(\frac{b}{a} + \frac{a}{b}\right)^2 \tag{2.3}$$

Timoshenko discusses rectangular plates with boundary conditions other than simply supported on all sides. However, for the case of clamped (fixed) on the loaded edges and simply supported on the others, only a table is provided for appropriate *k* values, shown as Table 2.1.

Table 2.1: Values of *k* for Loaded Edges Clamped Case, replicated from Timoshenko et al (1961)

a/b	0.6	0.8	1.0	1.2	1.4	1.6	1.7	1.7	1.8	2.0	2.5	2.8	3.0
k	13.38	8.73	6.74	5.84	5.45	5.34	5.33	5.33	5.18	4.85	4.52	4.50	4.41

Timoshenko references a paper written by F. Schleicher in 1932 which the author has been unable to locate. All other sources consulted related to rectangular plate buckling provide the same table without a closed-form function for *k*.

2.2.2 Oblique plate buckling

Yoshimura et al (1963) provide classical solutions to the buckling of oblique plates in their paper published in ASME's Journal of Applied Mechanics. The work presented in this paper is a continuation of work done by W. H. Wittrick, which examined fully clamped oblique plates subjected to uniform compression in both directions. The solutions presented by Yoshimura explored the elastic buckling of simply supported oblique plates with compression in one direction. This research stems from the aeronautical industry designing panels used in space or aircraft. The scenario in which Yoshimura is investigating is shown graphically as Figure 2.2.

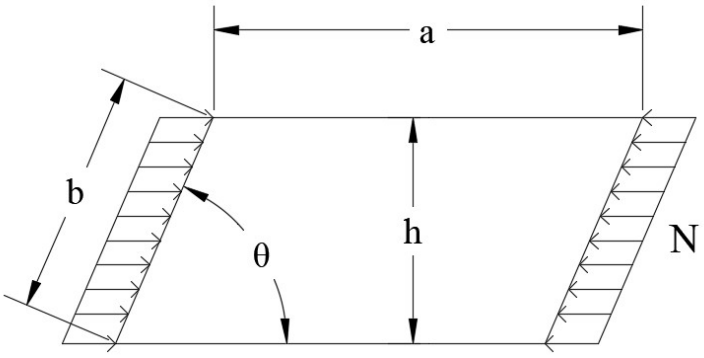

Figure 2.2: Oblique Plate Under Compressive Stress – Analogous to Yoshimura et al (1963)

Yoshimura's solution for the elastic buckling of simply supported oblique plates is derived using the principles of virtual work and conservation of energy during buckling. A function for the buckling coefficient *k* is determined through an eigenvalue analysis considering the number of buckled sine waves in the plate and the aspect ratio, like the one employed by Timoshenko (1961).

The solution presented by Yoshimura of the elastic buckling of the plate in Figure 2.2 is given by the following equation:

$$N_{cr} = k_c \frac{\pi^2 D}{a^2} \tag{2.4}$$

Where *D* is the same definition of plate rigidity as 2.2.1, and k_c is defined by the following:

$$k_c = \beta^2 \frac{\phi_{cr}}{\sin^3 \theta} \tag{2.4}$$

The term β in this case is the aspect ratio, a/b. The term ϕ_{cr} is obtained through a 5th order eigenvalue analysis of the dimensions of the plate. When θ is equal to 90 degrees, or in the case of a rectangular plate, and the aspect ratio is equal to 1, this value of ϕ_{cr} becomes 4. In turn k_c is equal to 4, representing the elastic buckling coefficient of an infinitely long plate rather than a rectangular one. In theory, this relationship could be modified to be compatible with the rectangular plate buckling solution provided by Timoshenko (1961) by setting k_c (Yoshimura) equal to k (Timoshenko) when θ is equal to 90 degrees. This hypothesis is discussed further in Chapter 7.

2.3 Inelastic Plate Buckling

Ziemian's book *Stability Design Criteria for Metal Structures* summarizes several theories and methodologies for determining the ultimate strength of a plate after buckling. The concept of effective width, b_e, is used throughout the different methodologies When plates buckle, stresses and strains redistribute to a lower energy form. This process creates a loss of stiffness in the regions that buckling occurs, primarily in the middle away from the supports. The edge regions close to the supports then attract most of the stress because those regions are stiffened the most against buckling. A diagram of the compressive stress distribution after buckling is provided in Figure 2.3.

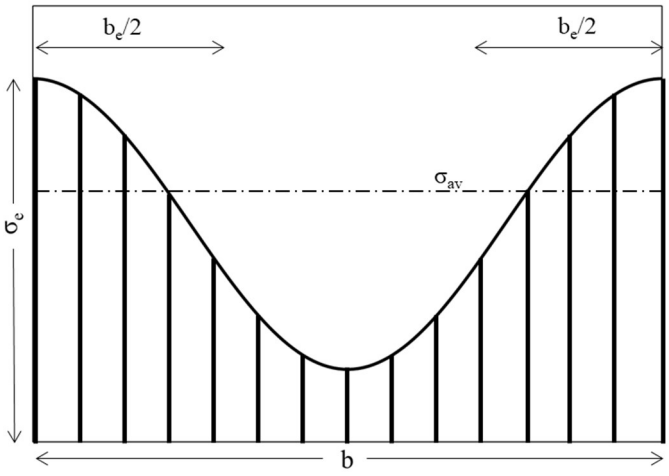

Figure 2.3: Compressive Stress Distribution after Buckling with Definitions of Effective Width and Average Stress. Adapted from Ziemian (2010)

Ziemian calls the use of the effective width concept in estimating the maximum strength of plates a "semiempirical method." He uses this term because many factors go into determining buckling strength, including the effects of residual stresses and geometric and material imperfections.

The first use of the effective width concept was von Kármán et al (1932). For plates under uniform compression, von Kármán developed the following equation for effective width.

$$b_e = \left[\frac{\pi}{\sqrt{3(1-\nu^2)}}\sqrt{\frac{E}{\sigma_e}}\right]t \tag{2.5}$$

More studies and tests were conducted to further refine this prediction for effective width. Winter (1947) conducted a series of such tests, specifically on thin steel compression flanges. He then suggested the following formula for effective width.

$$\frac{b_e}{b} = \sqrt{\frac{\sigma_c}{\sigma_e}}\left(1.0 - 0.25\sqrt{\frac{\sigma_c}{\sigma_e}}\right) \tag{2.6}$$

The term σ_c in Equation 2.5 is the critical elastic buckling stress. The primary difference between Equation 2.5 proposed by von Kármán et al (1932) and Equation 2.6 proposed by Winter (1947) is the addition of the 0.25 coefficient in Winter's equation. This constant is a correction coefficient reflecting the total contribution of various imperfections. Winter's Equation 2.6 was adopted by the AISI Specification for cold formed steel through 1962, until the coefficient 0.25 was changed to 0.22 in the 1968 edition (Ziemian 2010).

Ziemian modifies Winter's (1947) equation to represent the ultimate compression load of the plate by substituting the edge stress, σ_e, for the yield stress, σ_y. The left-hand side of the equation becomes the average membrane stress in the plate at ultimate load, σ_{av}, defined as the ultimate load divided by the cross-sectional area of the plate, $b*t$. The equation is then normalized by σ_y resulting in the following non-dimensional curve for the ultimate compression load in the plate (Ziemian 2010).

$$\frac{\sigma_{av}}{\sigma_y} = \sqrt{\frac{\sigma_c}{\sigma_y}}\left(1.0 - 0.22\sqrt{\frac{\sigma_c}{\sigma_y}}\right) = \frac{P_{ult}}{P_y} \tag{2.7}$$

Kalyanaraman et al (1977) conducted a similar analysis of the average stress at ultimate load. This study focused generally on unstiffened compression elements, not just compression flanges in cold formed steel members. This investigation yielded a similar conclusion, resulting in a similar equation.

$$\frac{\sigma_{av}}{\sigma_y} = 1.19\sqrt{\frac{\sigma_c}{\sigma_y}}\left(1.0 - 0.3\sqrt{\frac{\sigma_c}{\sigma_y}}\right) = \frac{P_{ult}}{P_y} \tag{2.8}$$

Both equations derived by Ziemian (2010) and Kalyanaraman (1977) represent the non-dimensional compression capacity of steel plates. The only difference between these equations is the correction coefficients used to calibrate the equation to a set of experimental data. Therefore, a general form of these equations could be written as:

$$\frac{\sigma_{av}}{\sigma_y} = A\sqrt{\frac{\sigma_c}{\sigma_y}}\left(1.0 - B\sqrt{\frac{\sigma_c}{\sigma_y}}\right) = \frac{P_{ult}}{P_y} \tag{2.9}$$

2.4 Room Temperature Creep of Steel

One of the more recent studies on the creep effects of steel comes from Brnic et al (2010) where the material properties of structural steel ASTM A709 was investigated. This paper published in ASCE's Journal of Engineering Mechanics presents findings of uniaxial tension creep tests at lower and elevated temperatures. ASTM A709 steel was determined to be "creep resistant" at low temperatures, following the common trend in high strength low alloy (HSLA) steels. Creep effects become significant at temperatures greater than 300 degrees Celsius.

3. EXPERIMENTATION

A series of experimental tests were conducted to provide a baseline for future numerical models. A total of 9 tests were conducted on segments of W18X40 wide flange sections of ASTM A992 Gr50 steel. Certified mill test reports (CMTR) of the W18X40 sections showed the specimens' yield and ultimate strengths to be 57 kips per square inch (ksi) and 75.5 ksi, respectively. The CMTR also showed the elongation at break to be 25 percent on average. Of the 9 tests, 3 "dummy" tests were performed to ensure the effectiveness of the test setup, followed by 2 monotonic load tests of a 42-inch specimen, 2 sustained load tests on 42-inch specimens, one sustained load test on a 32-inch specimen, and a monotonic load test on a 24-inch specimen. In the sustained load tests, the load was applied gradually up to 80 to 90 percent of the expected capacity and then held constant for several hours. After no creep buckling was observed, the load was increased gradually again until buckling occurred. The nomenclature of the official tests that were conducted, and whose results are reported in this paper, is described in the following table.

Table 3.1: Experimental Tests to be Conducted

Test Number	Section	Specimen Length (in)	Sustained Load Portion
1	W18X40	42	NO
2	W18X40	42	NO
3	W18X40	42	YES
4	W18X40	42	YES
5	W18X40	32	YES
6	W18X40	24	NO

3.1 Objectives

The experimental tests were designed to accomplish 2 specific objectives: obtain experimental data to benchmark numerical models and investigate any creep effects in the inelastic buckling of steel members. To provide adequate benchmarking, data was collected from the experimental tests, mainly displacements and strains. The experimental setup was also designed

to be easily replicated in the numerical model. The effect of sustained loads and creep buckling is investigated by carefully monitoring the load on the specimen for the duration of the test.

3.2 Test Setup

The test setup was designed to create testing conditions that can be easily replicated in the numerical model. The setup was also designed to ensure that the specimen buckled uniformly in a purely lateral mode (i.e. without twisting). To do so, the setup applied a uniform compressive load to the top flange of the specimen without allowing flange rotation. This setup only allowed the top flange to move vertically downward relative to the rest of the specimen, producing the desired buckling mode.

To accomplish these goals, larger, stiffer members were included in the setup to prevent flange rotation. The large elements were fixed in place so only vertical deflection of the top flange of the specimen was permitted. The bottom flange of the specimen was attached to a steel plate platform using 20 fully tensioned structural bolts. The platform was post-tensioned to the lab's strong floor. The top flange was similarly bolted to a large, built-up spreader beam. This beam's primary purpose was to provide an avenue for the applied force from the 250-ton vertical actuator to uniformly spread across the top flange of the specimen, thus the name "spreader beam." The spreader beam also prevented rotation in the top flange. The spreader beam was held in place by 2 lateral braces made of a stub column and a load cell. These braces were held in place using 4 threaded rods tied back to the load frame and then tensioned down to ensure a snug fit between all components. A schematic drawing of this initial setup is provided in Figure 3.1.

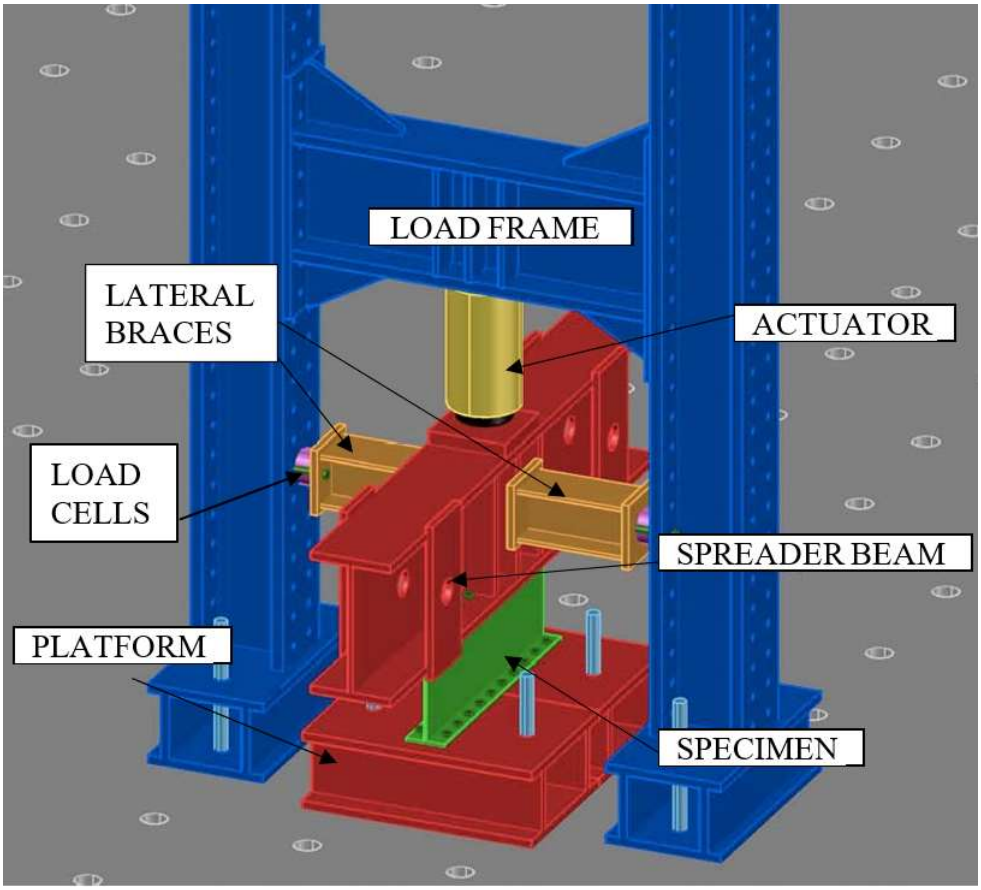

Figure 3.1: Schematic Drawing of Test Setup

Only one test was conducted using the setup in Figure 3.1. The commissioning test of this setup revealed a degree of torsional freedom allowing the entire setup to twist about a vertical axis. This problem was corrected by installing additional braces that prevent the ends of the spreader beam from moving in the out-of-plane direction. These braces were H-shaped frames made of steel W8 sections. The entire frame was post tensioned to the lab floor to provide a strong base reaction. Teflon plates were added to the contact points between the end brace and the spreader beam to prevent any significant frictional force from developing. This setup was also able to accommodate the different sized specimens. A picture of the final test setup is shown in Figure 3.2.

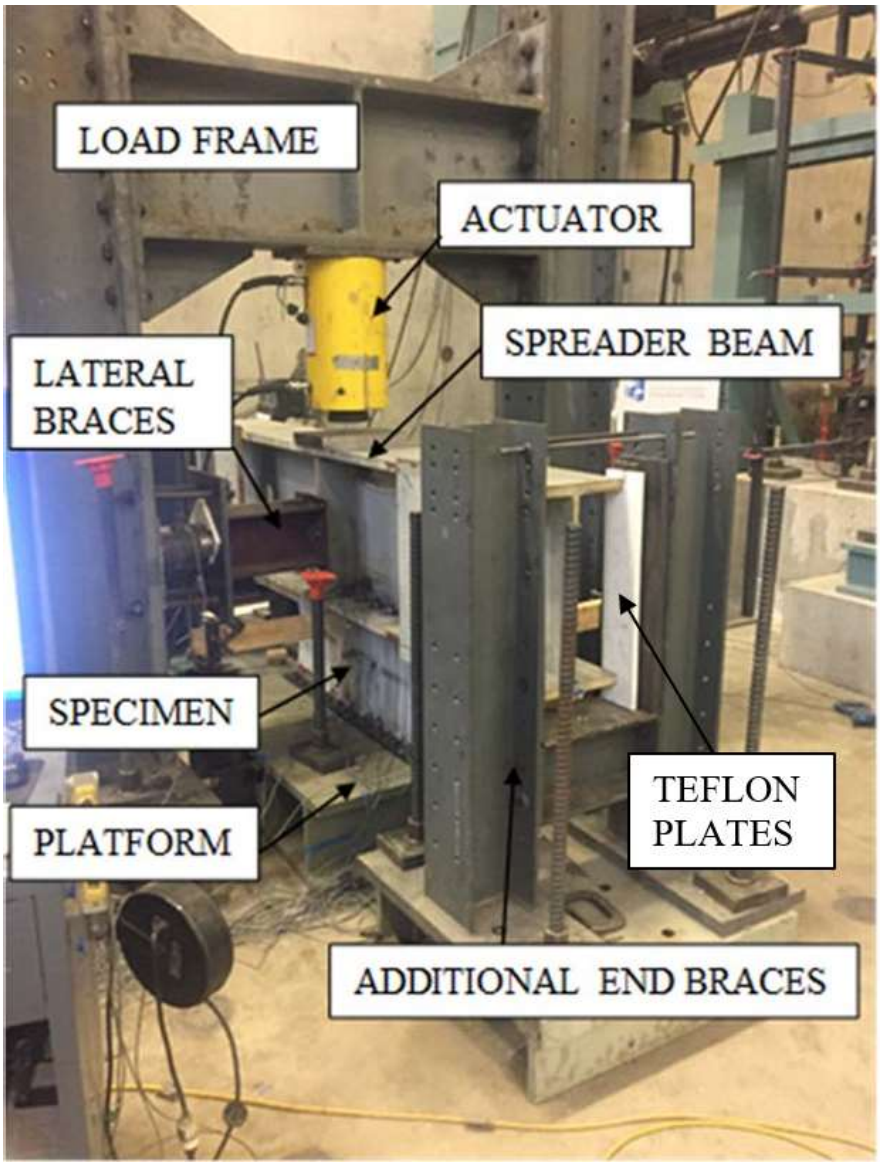

Figure 3.2: Completed Test Setup

3.3 Instrumentation

Instrumentation was used for 2 purposes: to measure the critical deformations in the specimen under the applied load, and to ensure the test setup was working correctly by not allowing unwanted displacements and rotations. Both displacements and strains were measured. The vertical displacement of the top flange and horizontal out-of-plane (OOP) displacement at the midpoint of the web were measured. Initially, string pots were used to measure these displacements, but due to the extremely small magnitude of displacements, the sensors were changed to low voltage displacement transducers (LVDTs). Vertical strains were captured in the specimen through

5mm strain gauges. Inclinometers were attached to either end of the spreader beam to track any rotation of the top flange. This rotation was assumed to be greater than or equal to the rotation in the top flange because of the much higher stiffness of the spreader beam. Load cells in the lateral braces provided information on how much force was required to keep the setup straight. A graphical depiction of the first sensor layout with string pots is provided in Figure 3.3.

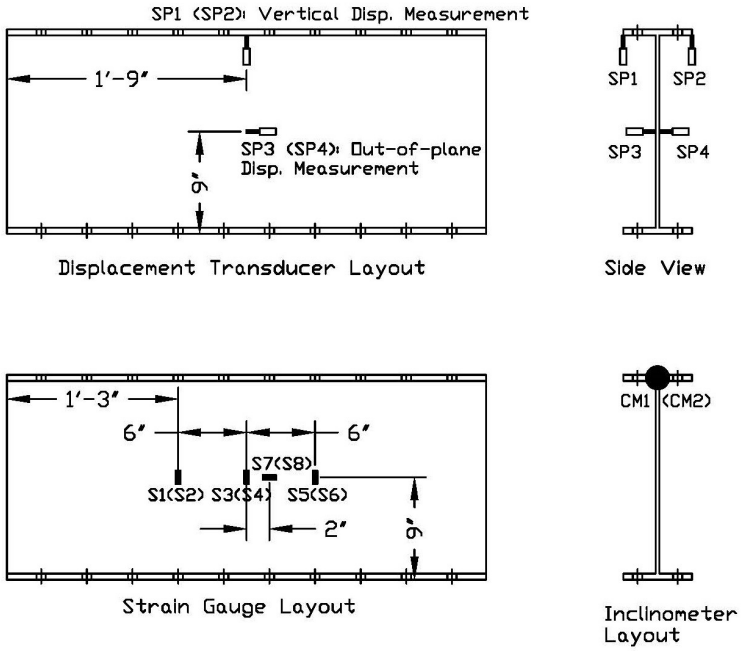

Figure 3.3: Initial Instrumentation Layout

A total of 8 strain gauges (shown as S#) were applied to the web of the specimen along the mid-height. Vertical gauges were applied at the midpoint and at a distance of 6 inches to either side of the midpoint. Transverse (horizontal) gauges were also applied near the midpoint at 2 inches away from the vertical gauge. This layout is mirrored on both faces of the web. The inclinometer (CM) was not applied directly to the specimen but rather was attached to the spreader beam.

After the first commissioning test, additional sensors were added to measure vertical displacement of the top flange of the specimen. The two LVDTs in the out-of-plane direction were redundant, so one of them was removed. Additional LVDTs were added to the top flange to capture any variation along the length of the specimen, and the new layout is provided in Figure 3.4.

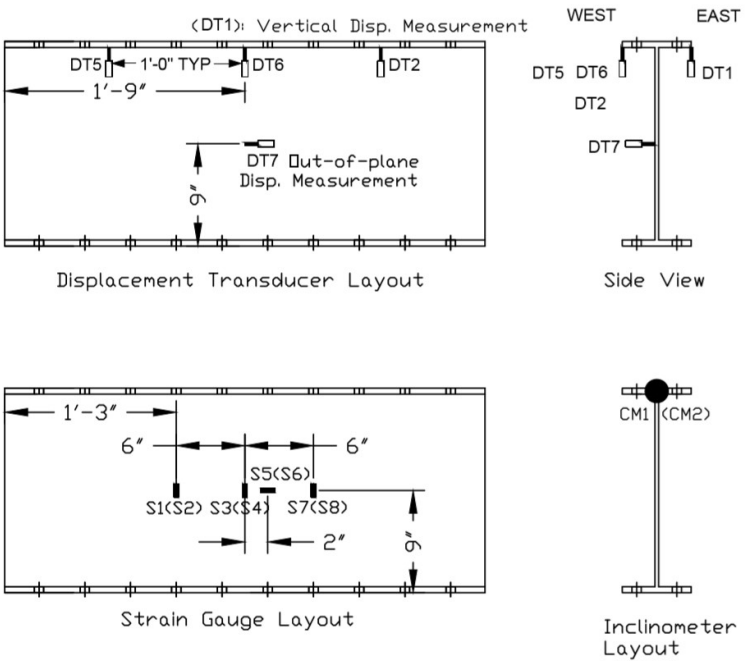

Figure 3.4: Instrumentation Layout for Tests 1 and 2

The first two reportable tests were conducted with this layout. After examining the results, the instrumentation plan was adjusted for tests 3 and 4. Additional LVDTs in the out-of-plane direction were added along the length of the specimen at the same points where vertical sensors already were placed. Additionally, the platform supporting the specimen was experiencing its own deformations in response to the large reaction forces required. The deformations in the platform defied the assumption that the bottom flange experienced zero displacement. To correct for this displacement, more LVDTs were added to measure the deflection of the bottom flange directly underneath the ones measuring the top flange. These additional sensors allowed for the net flange displacement to be calculated. In addition to the added LVDTs, 4 more strain gauges were added near the ends of the specimen, two on each face. These LVDTs were added to determine if the load from the actuator was more concentrated in the middle of the specimen. The resulting instrumentation layout after these changes is shown in Figure 3.5.

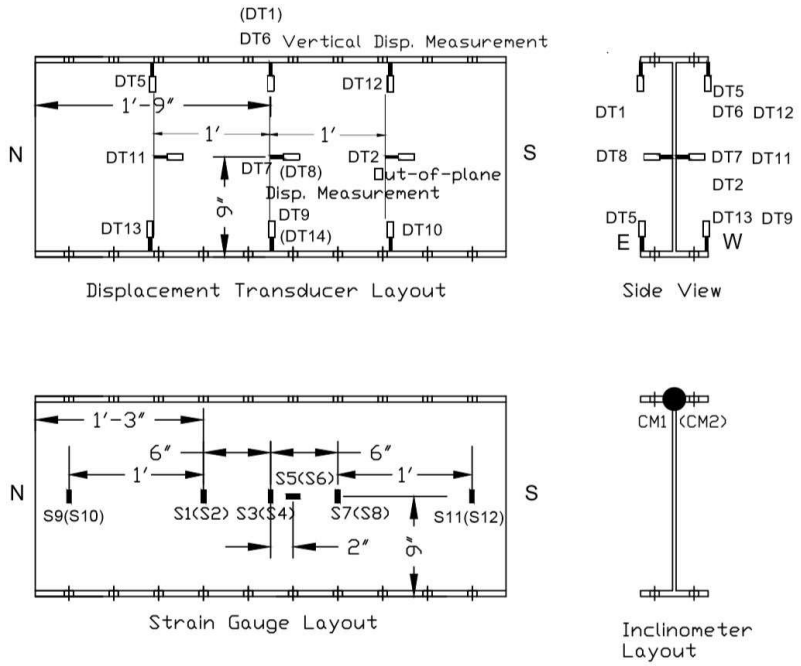

Figure 3.5: Instrumentation Layout for Tests 3 and 4

The above instrumentation layout was also used for the tests with shorter length specimens. The strain gauges at the ends were kept at 3 inches away from the edge of the specimen rather than 12 inches from the next closest gauge.

3.4 Loading Protocol

The monotonic loading was a simple protocol where the load was applied and increased quasi-statically until buckling. These tests were done first to provide a baseline for the expected strength and behavior of the specimens. This information was then used in deciding when to stop and sustain the load in future tests.

The next 3 tests involved a sustained load protocol. The tests started out exactly like the monotonic tests, but the load was sustained when certain load levels were reached. The target load was 80 to 90 percent of the final buckling load, but determining this load ahead of time was difficult due to the high variance observed in Tests 1 and 2. However, a reversal of strains on the face of the web from compression to tension was consistently observed prior to buckling. The load at which this reversal occurred was used as the sustained load level.

3.5 Measured Imperfections in Test Specimens

Consistent with nearly all buckling analyses, the initial imperfection in the system plays a role in the overall behavior. In this series of tests, the critical imperfections were those affecting the shape of the web. This determination was made after the first official test, and measurements were taken for Tests 2-6. This data was not used directly in the construction of the numerical models, but instead used to provide insight on the buckling strength of the specimen. For instance, if one specimen failed at an applied load of 340 kips and had measured imperfections in the web of 0.05 inches, another specimen with measured imperfections of 0.07 inches should fail at a load less than 340 kips. However, it was not clear how to determine the magnitude of imperfections present in the specimen webs from examining standards and codes alone. ASTM A6, which governs the manufacturing tolerances of wide flanged sections, does not provide a direct discussion of out-of-plane imperfections in the web of these members. Nevertheless, out-of-plane imperfections were measured in the webs of the specimens using the technique described in Section 3.5.1.

3.5.1 Measurement technique

To measure out-of-plane imperfections, the "perfect" reference plane must be established. This plane was defined as a straight line connecting the ends of the flanges extended along the length of the specimen. With this reference plane, a straight edge and a caliper was used to take measurements from that plane to the face of the web, creating a topography of the web surface. This technique is depicted in Figure 3.6.

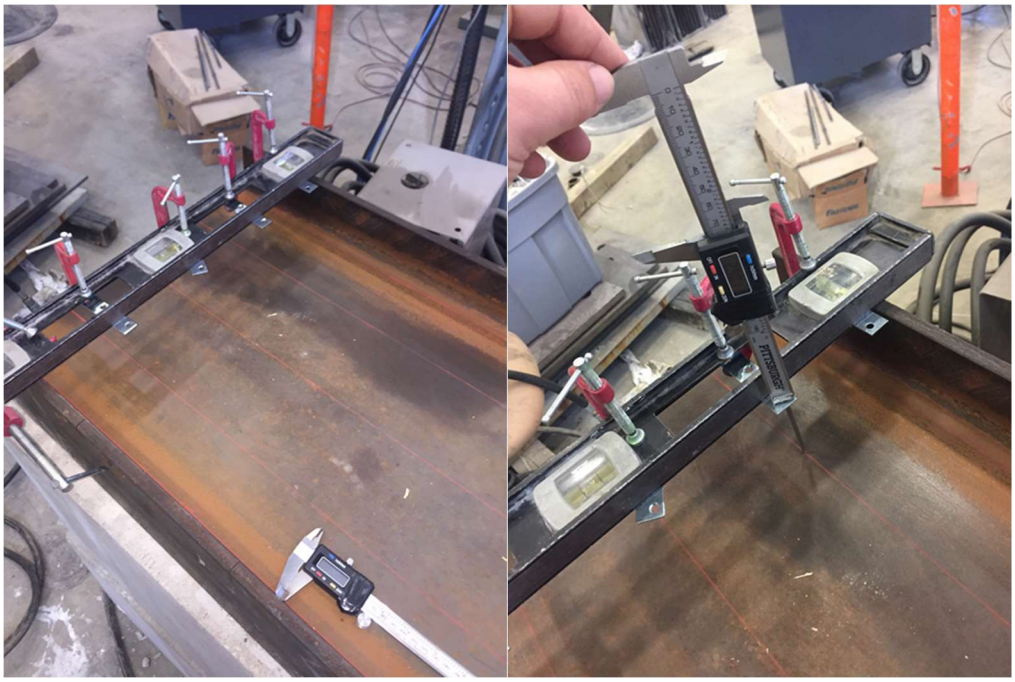

Figure 3.6: Initial Out-of-Plane Measurement Technique

3.5.2 Results

The straight edge is set to take measurements at the ends and quarter points of the specimen for a total of 5 locations along the length. At each of these locations, measurements were taken at the ends of the fillet and quarter points along the depth of the web for a total of 25 points. The maximum of these measurements was defined as the initial web imperfection; some results are shown in Figure 3.7.

The results of this measurement technique are not necessarily applicable to all sizes wide flange shapes. The measurements were taken on one heat of W18X40 beams manufactured at Steel Dynamics Inc. in Columbia City, Indiana and therefore could contain imperfection properties that are unique to this manufacturer. Further investigations could be done considering a wider variety of wide flange shapes from multiple manufacturers to provide more comprehensive data regarding the out of plane imperfections in the webs of wide flange sections.

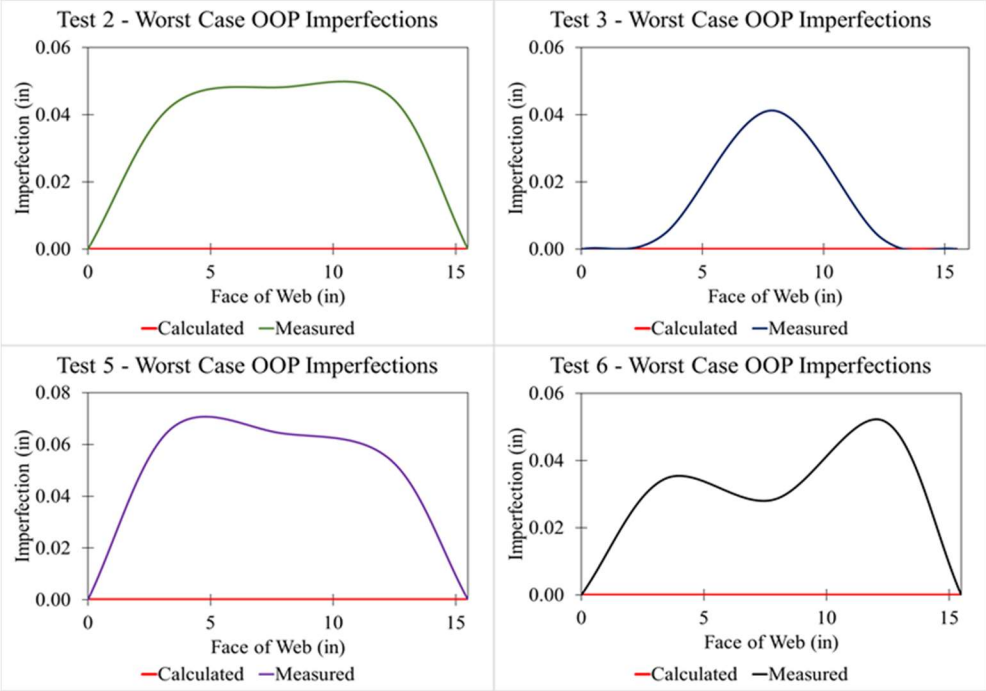

Figure 3.7: Measured Results of Initial Out-of-Plane Imperfections in Test Specimens

The preceding plots are the largest measured imperfections in the webs of the tested specimens. The lines represent one location along the length of the specimen (either the midpoint or one of the quarter points) where measured out-of-plane imperfections was the greatest. The x-axis represents the face of the web, varying from zero at the top to 15.5 inches, the fillet to fillet height, and the y-axis is the measured imperfection in inches. The plots of the imperfection all take on different shapes, thus eliminating any conclusion that could be drawn about future specimens. The maximum imperfection measured in the specimens was in Specimen 4 at 0.071 inches or $0.23*t_w$. The average of all measurements taken was 0.041 inches or $0.13*\ t_w$. A complete table of results is shown below.

Table 3.2: Measured Out-of-Plane Imperfection in Test Specimens

Specimen	Length (in)	Max Imperfection (in)	(% of t_w)
2	42	0.048	15%
3	42	0.041	13%
4	42	0.071	23%
5	32	0.066	21%
6	24	0.052	17%
	Average:	0.041	13%

4. NUMERICAL MODELING

The purpose of the first phase of numerical modeling was to identify potential shortcomings of the test setup and further confirm the setup's effectiveness. The numerical models were developed in the commercial finite element software ABAQUS using their 3D solid element library. Multiple ABAQUS models were developed over the course of the testing phase. The goal of the numerical models was to replicate the procedure and results from the experimentation as a benchmark for a parametric study of many cases. The accurate replication of the experiments provided confidence in the model's ability to accurately predict cases that were not explicitly tested.

4.1 Replication of Experiments

4.1.1 Model creation

The first set of models created were direct replicas of the experimental setup, shown in Figure 4.1. The model included the spreader beam and the platform pieces as well as the specimen to capture any minute effect the components might have on the test results. The reduced integration solid element C3D8R was used throughout with a very fine mesh density. The C3D8R is a general purpose linear solid element with reduced integration, allowing it to model all the different parts with a good degree of accuracy. The boundary conditions were prescribed as points of zero displacement, such as the surface of the strong floor and the brace points on the spreader beam.

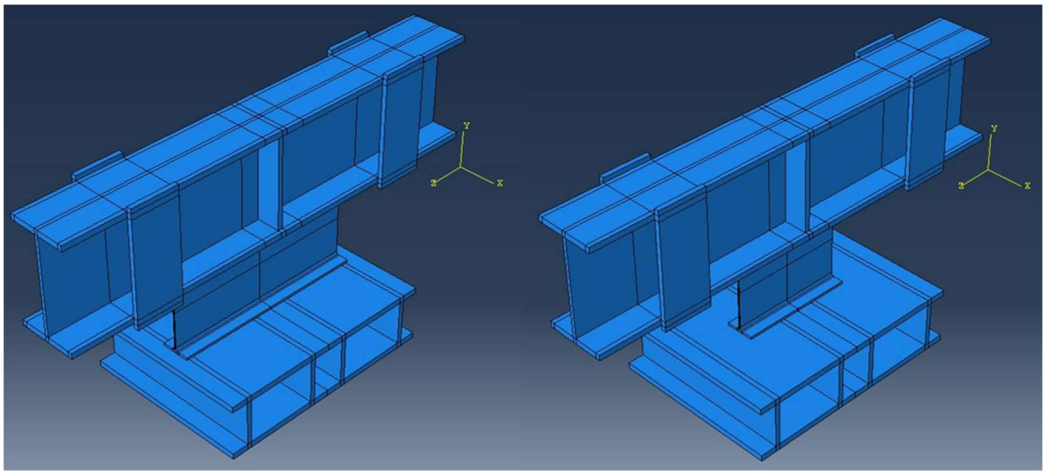

Figure 4.1: ABAQUS Model Assembly for Replicating Experimental Tests

A 0.2” mesh size was used in the specimen with 4 elements through the thickness of the web while a 1” mesh size was used in all other parts in the model. The specimen was created by extruding the W18X40 section to the desired length. The section sketch was created using the design dimensions from the AISC Manual and directly modeled the fillet between the web and the flange, shown graphically in Figure 4.2. The steel material used in the analyses was defined according to multiaxial plasticity theory with Von-Mises yield surface and isotropic hardening. The elastic modulus was set as 29000 ksi and Poisson’s ratio was set to 0.3. The stress-strain relationship was defined according to the certified mill test reports from the manufacturer, which provided a yield strength of 57.11 ksi, ultimate strength of 75.5 ksi, and 8% elongation at break.

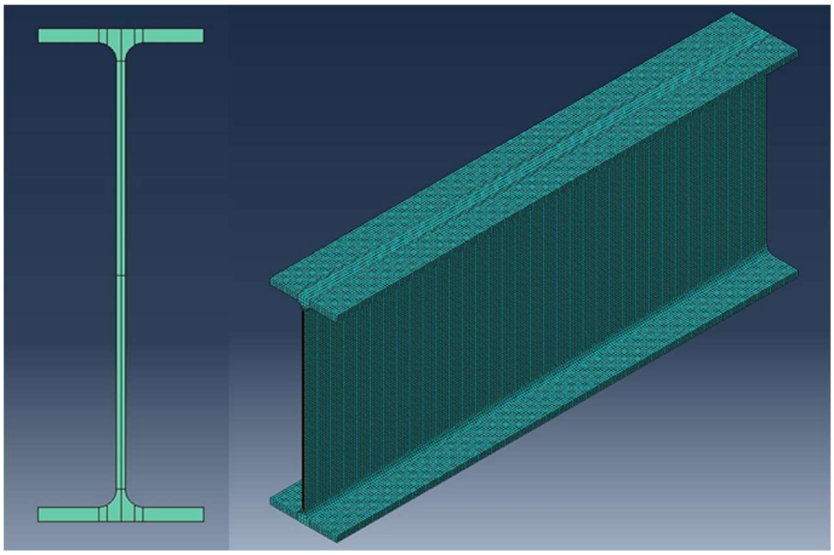

Figure 4.2: Specimen Used in ABAQUS Models

4.1.2 Analysis procedure

The analyses were performed using the ABAQUS/Standard solution method. The models were tested using sequential analyses. First, a linear perturbation buckling analysis was performed to obtain the critical elastic buckling load and the critical buckling modes via an eigenvalue analysis. A unit vertical load was applied as a uniform pressure over an area equal to the actual contact area of applied force in the experiments. The displacement results of this buckling analysis were saved in an ABAQUS .fil file and used to apply imperfections in the web. A value of initial imperfection was applied to the first eigenmode shape to obtain the greatest effect and to most accurately model the buckling shape of the experiments. This magnitude is not necessarily the magnitude of the measured imperfection of a given specimen because the shape pattern of the

imperfections would be very different. The specimens have essentially a random shape to their imperfection, while the imperfections in the numerical models would follow the critical buckling mode. A static Riks analysis considering nonlinear geometry and these geometric imperfections was then conducted to obtain the final buckling strength.

Analyses were conducted with many different amplitudes of initial imperfection by varying the peak imperfection value by a factor of 5%-30% of the web thickness (0.05-0.3*t_w). This range corresponds to 0.01575 to 0.0945 inches of imperfection for a W18X40 specimen. Residual stresses were not considered in these analyses because their direction of influence is primarily along the longitudinal axis of the beam and thus have minimal influence in the direction of loading in this case.

The ABAQUS modified-Riks analysis was used to capture the pre- and post-buckling responses of the specimen. The history output from the analysis was compared with the corresponding sources of experimental data. This comparison is shown as a field of curves representing the experimental results and numerical results of varying imperfection levels

5. EXPERIMENTAL RESULTS AND COMPARISONS

The contents of this chapter are paraphrased from “On the influence of load width on web compression buckling strength” by Sener et al (2019).

5.1 Commissioning Tests

The results of the commissioning tests were used to determine the effectiveness of the test setup rather than the strength of the specimen. The mode shape of the final buckling failure is very important and contributes greatly to the final strength of the specimen. The experimental tests should produce failures in the desired buckling mode, and the commissioning tests were intended to prove this hypothesis. The first commissioning test revealed a torsional instability not addressed in the original setup. Instead of a uniform lateral buckling along the length of the specimen, the torsional mode was activated first. This failure shape is shown in the following Figure 5.1.

Figure 5.1: Photos of Commissioning Test 1 Showing Undesired Torsional Buckling

This unwanted torsion was addressed by adding the steel end braces shown in Figure 3.2. These braces were added to ensure the desired buckling mode was reached. The second commissioning tests with the end braces produced the desired buckling mode, shown in Figure 5.2.

Figure 5.2: Photo of Commissioning Test 2 Showing Desired Buckling Shape

5.2 Monotonic Loading Only

The results of the monotonic loading were compared with numerical model simulation. In the tests that contained sustained load, the monotonic portion was extracted and used in the comparison as well. The failure load was determined from both the experiments and the numerical simulation and summarized in the table below. The nominal strength calculated in accordance with AISC equation J10-8 is also provided in a footnote. The mean strength of the tested specimens is 341 kips with a 4% coefficient of variation.

Table 5.1: Summary of Experimental Test Results of 42" Specimens

	Experimental		Numerical	
Test	Observed Strength (kips)	Percent of Strength Sustained	Initial Imperfection	Predicted Strength[1] (kips)
1	341.3	-	$0.1t_w$	365.5
2	359.3	-	$0.2t_w$	346.6
3	342.8	91	$0.3t_w$	327.6
4	320.1	83		

[1] *AISC Eq J10-8 Predicted Strength: 60.3 kips*

Figure 5.3 and Figure 5.4 graphically show the comparison of the experimental tests to the numerical analysis in the form of load versus displacement and load versus strain graphs.

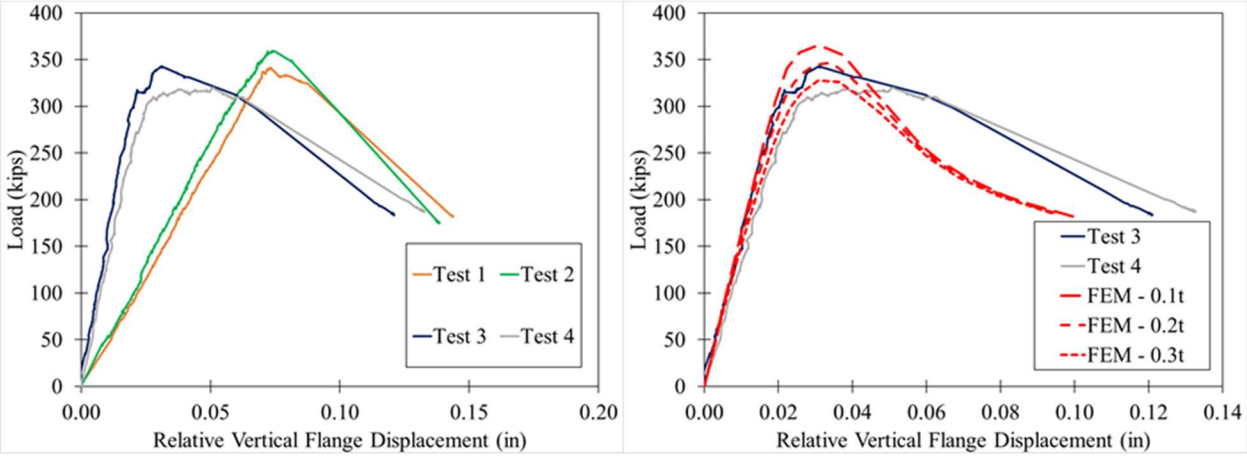

(a) (b)

Figure 5.3: Plot of (a) Experimental Vertical Flange Displacement Data and (b) Comparison of Vertical Flange Displacement Data

Figure 5.3 shows the vertical flange displacement response of the 42-inch specimens with respect to increasing load. Figure 5.3(b) shows the data obtained from the finite element modeling for different levels of initial imperfection. The imperfection levels were normalized by the thickness of the web, t_w, shown in the legend as 0.1t for 10% of the web thickness, etc. This nomenclature is repeated throughout. Figure 5.3(a) shows the experimental data gathered from all 4 tests shown as solid lines of various colors. The data in Tests 1 and 2 was gathered using the original instrumentation layout that only measured the vertical displacement of the top flange assuming the displacement of the bottom flange was zero. As discussed earlier in Section 3.3, this assumption is invalid, and the bottom flange displacement should be subtracted away from the top flange measurement. This error causes the perceived stiffness of the specimen in the vertical direction to be much lower than the real stiffness. Tests 3 and 4 corrected for this error in measurement, and their comparison to the numerical data is shown in Figure 5.3(b).

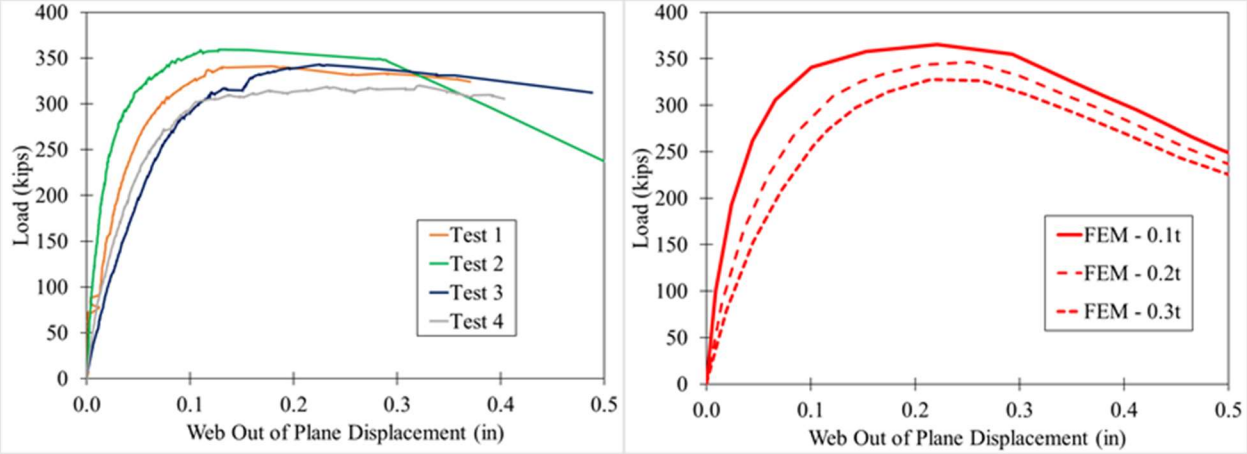

(a) (b)

Figure 5.4: Plot of (a) Experimental Web Out-of-Plane Displacement Data and (b) Numerical Web Out-of-Plane Displacement Data

This set of plots shows the out-of-plane (OOP) web displacement response in the 42-inch tests. Figure 5.4(a) is recorded experimental data, while Figure 5.4(b) is the numerical data for varying levels of imperfection in the web shown as red solid and dashed lines. For clarity, the two sets of data are shown separately here, and the combined plot is shown below in Figure 5.5.

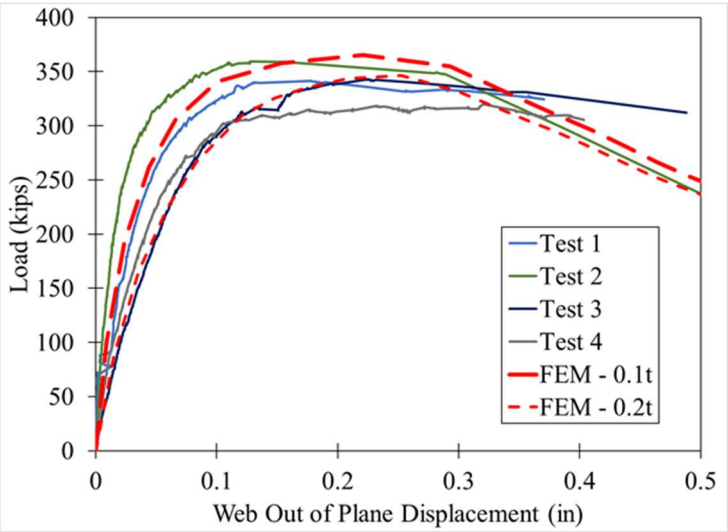

Figure 5.5: Comparison Plot of Web Out-of-Plane Displacement Data

The strains at the midpoint of either face of the web were also compared with the numerical results. The color pattern is the same as above, with the experimental results featured as several solid lines of different colors while the numerical results are shown as red dashed lines. The

experiments closely align with the numerical results generated with initial imperfections of $0.1t_w$ and $0.2t_w$.

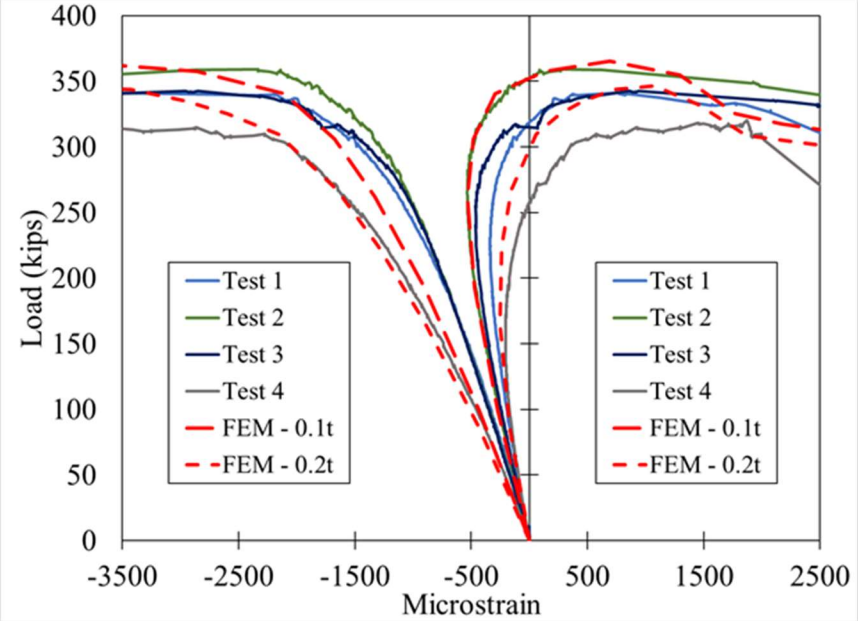

Figure 5.6: Comparison Plot of Vertical Strain Data

Some observations are drawn from examining the plots of strains. All four specimens experienced buckling shortly after 2 criteria were met: (1) one side experienced compression yielding, and (2) the other experienced the full strain reversal back to tension. This observation is justified by examining the mechanics of the web plate.

As more load is applied, the web of the specimen deflects in the out-of-plane direction as shown in Figure 5.7, resulting in a second order P-δ moment. This P-δ moment must be resisted by a bending moment in the web plate of the specimen to maintain equilibrium.

The moment and curvature caused by this P-δ effect changes the strain profile in the web as shown in Figure 5.7. The curvature (φ) induced due to the second-order effects causes the difference in strain between the surfaces of the web to increase as well.

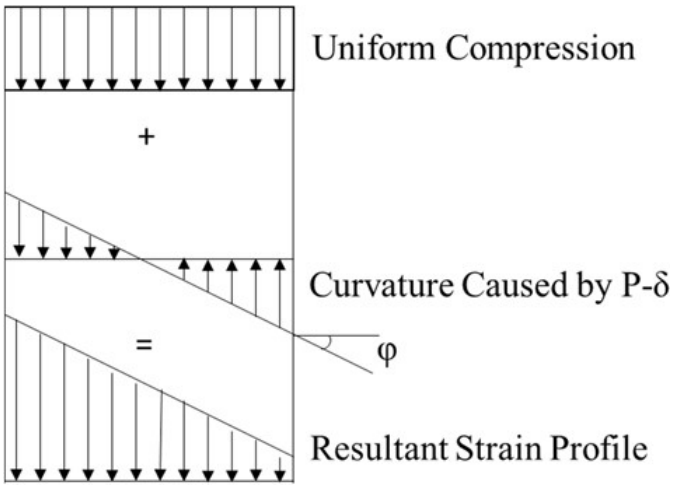

Figure 5.7: Theoretical Strain Profile in Web

This increase in curvature will continue as the compressive load increases until the specimen experiences a strain profile like the one shown in Figure 5.8. The strain profile prior to yielding changed proportionally throughout the thickness of the web, allowing the specimen to resist additional load. This change remained proportional because the steel in the web was still in the elastic range. Once the extreme compression fiber reached yielding, the inability of the yielded fibers to resist additional stresses caused instability and buckling of the web.

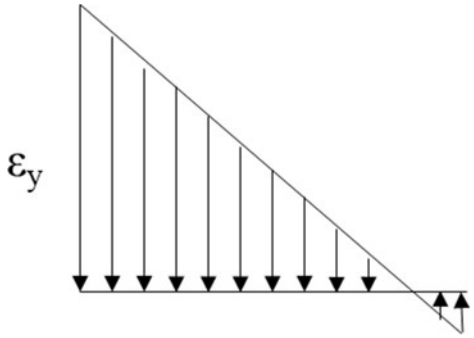

Figure 5.8: Theoretical Resultant Strain Profile at Buckling

5.3 Tests with Sustained Load

Figure 5.9 shows the strain responses over time from the sustained load portions of Tests 3 and 4 in parts (a) and (b) respectively. The blue/gray lines represent the vertical strain at the midpoint of the web while the yellow and red lines show the load over that same time, plotted on

a secondary axis. The decision to sustain a certain load level was made when the strain on the would-be tension side of buckling completed the reversal back to tensile strain at the face. This reversal was found to be an indication that buckling was imminent as discussed in the previous section. The load was sustained for a period of 150 minutes and 240 minutes in Tests 3 and 4 respectively.

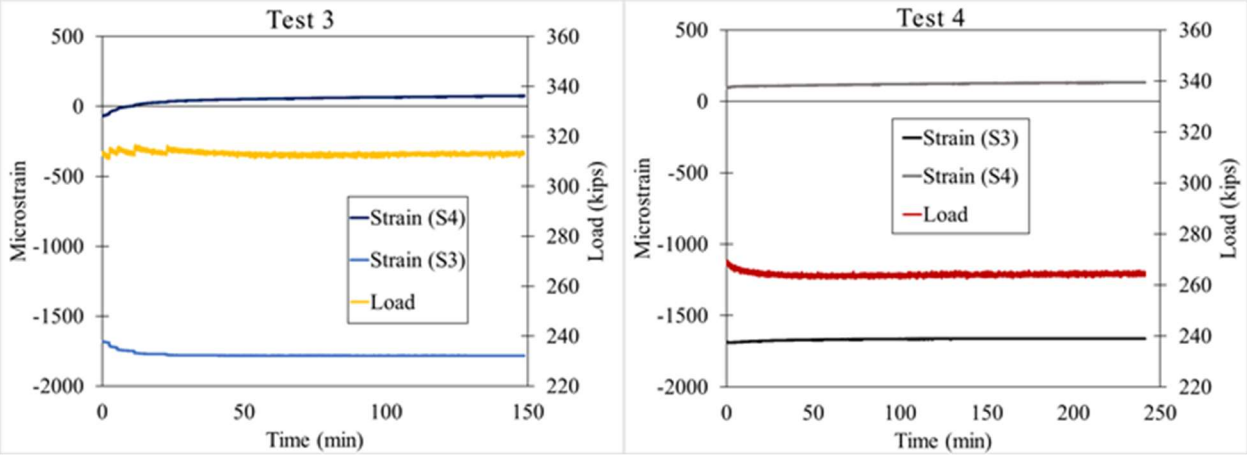

(a) (b)

Figure 5.9: Plot of Strain over Time in (a) Test 3 and (b) Test 4

The strain-time relationship plots show no significant creep strains induced by sustaining the load for the 4-hour period. Some irregularities at the beginning of the time period in Test 3 were caused by correcting for perceived relaxation in the hydraulic cylinder used to apply the load. By continuing to correct for this relaxation, the actuator was pushed further out and causing more displacement and strain in the system. In Test 4, no attempt was made to correct the pressure reading, and this produced a smoother plot. Both plots show no time dependent creep effects associated with web compression buckling. Test 5 also featured a sustained load portion, but due to a sensor malfunction during the sustained duration, the measured data contained large errors and is not presented.

5.4 Tests on Shorter Specimens

The experimental results from Tests 5 and 6 were also compared with appropriate numerical simulations. The net vertical flange displacement, web OOP displacement, and midpoint strain data were recorded and used in developing plots like those in the previous section.

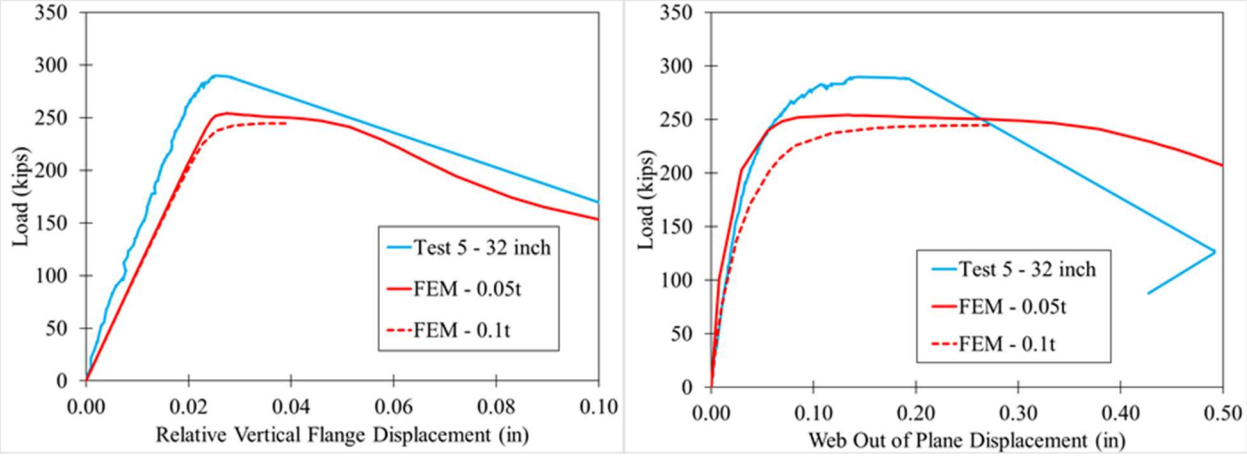

(a) (b)

Figure 5.10: Plot of Test 5 (a) Vertical Flange and (b) Web OOP Displacement Results

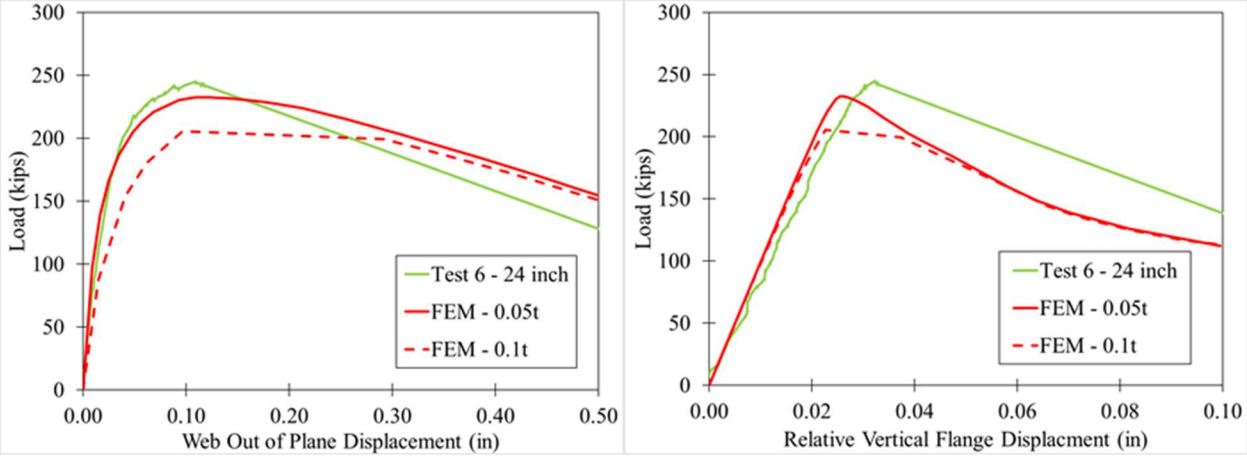

(a) (b)

Figure 5.11: Plot of Test 6 (a) Vertical Flange and (b) Web OOP Displacement Results

The above figures show the load versus displacement results for Tests 5 and 6. The numerical simulations that most represent the experimental data come from a lower magnitude of imperfection than in the longer specimens. This relationship is observed because the measured imperfections in specimens 5 and 6 were lower than the imperfections in their 42-inch counterparts. Additionally, the numerical models tend to underpredict the final strength of both tests. This variance in results is likely due to the variance in material properties of the specimens that are not accounted for in the numerical analysis. As the specimens get shorter, the likelihood of capturing material properties different than the average increases.

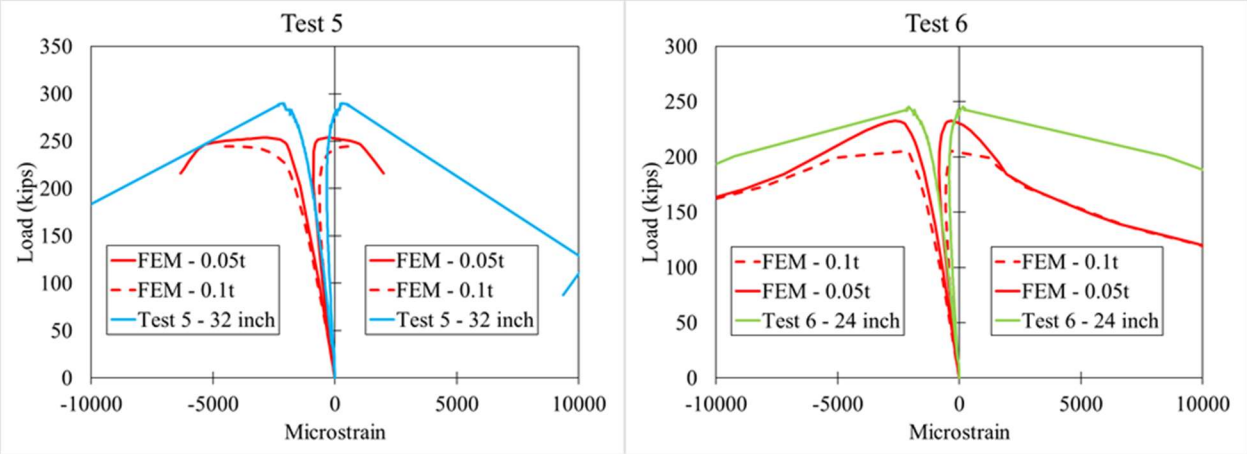

(a) (b)

Figure 5.12: Plot of Vertical Strain Results from (a) Test 5 and (b) Test 6

Figure 5.12 shows the strain response of Tests 5 and 6 along with their comparisons to the numerical models. Like the displacement plots previously, these plots also show the models underpredicting the strength of the experimental specimens. Just like in the 42-inch specimens, the completion of the strain reversal back to tensile strain on one face of the web is a strong indicator of buckling as the maximum experimental capacity is achieved shortly after that benchmark is reached.

6. NUMERICAL PARAMETRIC STUDY

After obtaining experimental data and developing models that accurately predict the response, a parametric study was conducted. The objective of this study was to provide numerical data to develop a prediction method that can be performed by hand. The parameters investigated include the section depth and thickness of the web, loaded width, and angle of applied load away from vertical. The variation in section dimensions was accounted for by investigating 4 common wide flanged beam sections of different web slenderness (h/t_w) ratios: W18X40, W18X60, W16X26, and W24X84. Each beam section was be subjected to load widths as a function of their section depth, d, ranging from 0.5d to 2.5d by increments of 0.5. 3 angles of application, θ, were also investigated: 0, 30, and 45 degrees measured from vertical (i.e. perpendicular to the specimen flange). These bounds are summarized in the following table.

Table 6.1: Parameters Investigated

Parameter	Values				
Section	W18X60	W24X84	W18X40	W16X26	
h/t_w	38.7	45.9	50.9	56.8	
w	0.5d	1.0d	1.5d	2.0d	2.5d
θ	0	30	45		

6.1 Model Creation

This parametric study varied from the previous models as only the specimen itself was modeled in a way that mimics typical construction applications like the details shown in Figure 1.3, Figure 1.4, and Figure 1.5. This change in purpose resulted in modifications to the model. The model used in the parametric study consisted only of the beam specimens subjected to the load. The spreader beam and platforms were removed and replaced with the appropriate boundary conditions. The load was applied by creating a rigid surface on the top flange of the specimen and applying a unit load to the centroid of this rigid plate. The width of the rigid plates was equal to the load width of the case investigated. The rigid plate at the opposite flange was held in place by a pinned boundary condition at the reference point. The top and bottom rigid plates were restrained against rotations and translations in the out-of-plane direction. Additionally, translations in the

longitudinal direction of the beam and in the out-of-plane were restricted at the area of load application. This boundary condition ensured translations were only in the vertical direction, perpendicular to the axis of the beam. Field conditions of these types of connections were assumed to restrain the web compression buckling region in this way. The specimens had a total length of 10 times the loaded width, *w*, being investigated with the purpose of minimizing the effects of different end conditions.

C3D20R solid elements were used rather than the C3D8R used previously. The C3D20R is a 20 node, quadratic, reduced integration solid element chosen for its ability to capture buckling. The element's quadratic shape function with 20 nodes allows for a coarser mesh without sacrificing accuracy in the analysis, thus increasing the computational efficiency. This element also rarely experiences hour-glassing, making the element useful in a buckling analysis. These changes were validated through additional benchmarking with the experimental results.

6.1.1 Parametric model benchmarking

These new numerical models must also be benchmarked with the experimental results. In the benchmarking stage, the specimens and loading were modeled to mimic the experiments. The specimens were modeled to the appropriate lengths and the rigid plate was extended to the entire top flange of the specimen. The material properties in the benchmarking models were defined according to the CMTRs of the experimental specimens described previously. The model used in the benchmarking is shown in Figure 6.1.

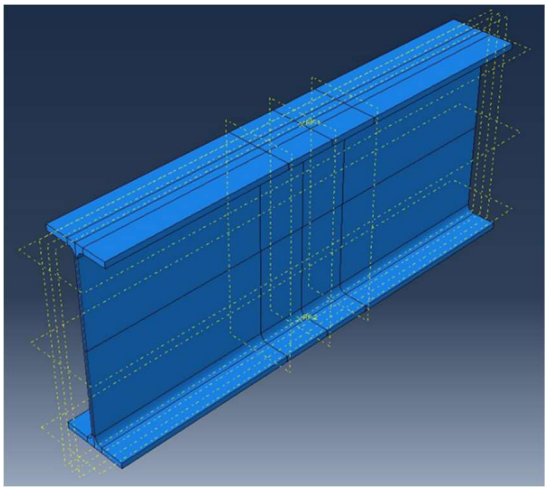

Figure 6.1: ABAQUS Model Used in Benchmarking

Analyses were performed to evaluate the element selection and mesh size. These analyses used the same sequential modified Riks approach as before. Results of this examination are shown in Figure 6.2.

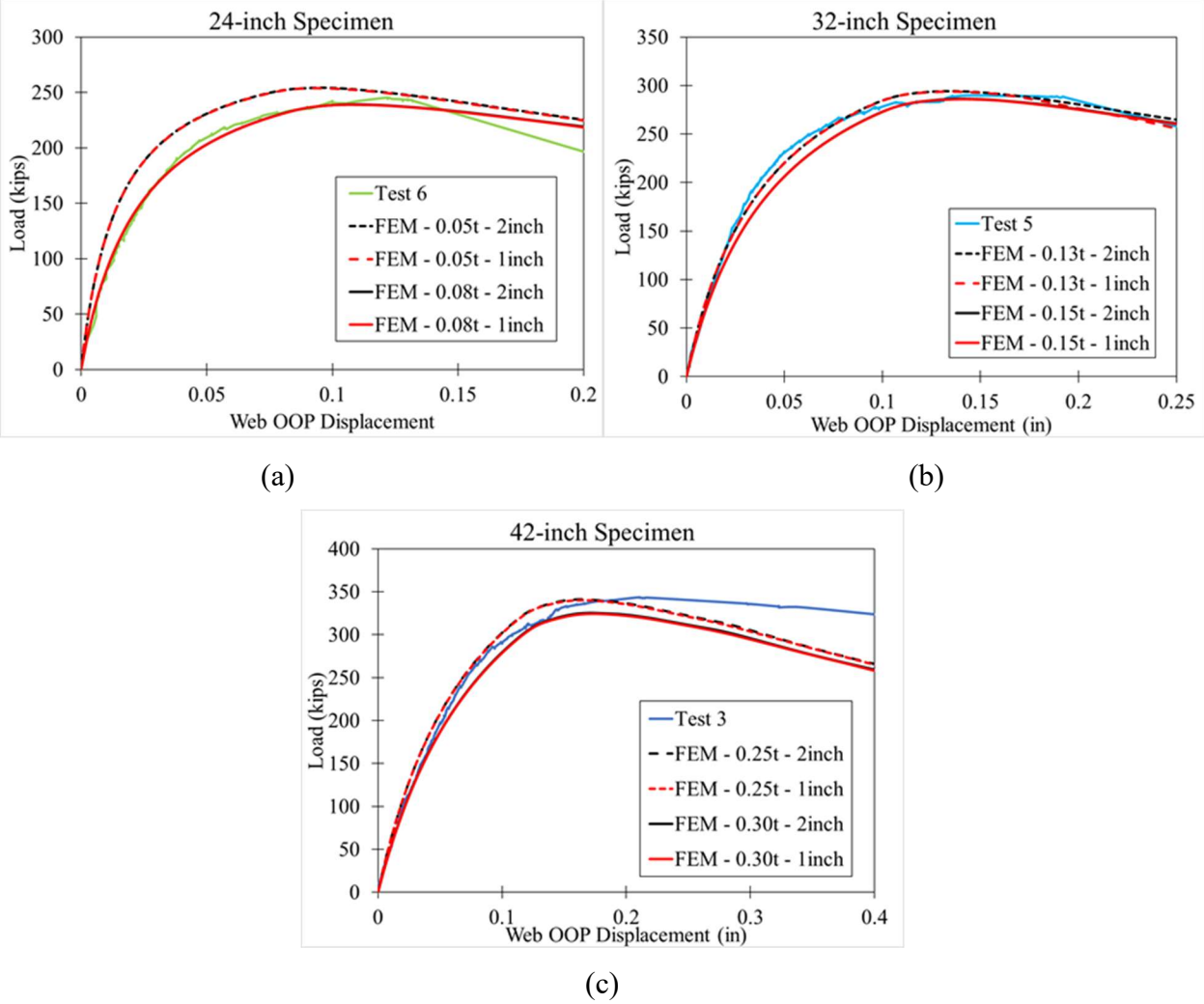

Figure 6.2: Comparison of Parametric Study Benchmarking Results to Experimental Results from (a) Test 6, (b) Test 5, and (c) Test 3

The load versus out-of-plane (OOP) displacement plots generated in the analysis are almost identical to the experimental data, both in terms of stiffness and final strength. The most accurate curves have a prescribed initial imperfection slightly lower than the measured value described in Table 3.2. This difference is because the imperfections applied to the numerical model followed the shape of the critical buckling mode, thus maximizing their effect. The imperfections measured in the real specimens were not associated with any shape and therefore are not as impactful as

imperfections along the critical buckling mode shape. The load versus displacement curves for a 1-inch and 2-inch mesh size were identical in all 3 plots. The black lines representing the analysis with 2-inch mesh were completely covered by the red lines representing 1-inch mesh. Therefore, the 2-inch mesh size will accurately predict the behavior of the specimen at a much lower computational cost.

6.1.2 Generating models to be used in the study

ABAQUS jobs were created for both steps in the modified Riks analysis procedure for all combinations of parameters being investigated for a total of 120 analyses. For each analysis, a model was created with the same process described earlier with a section sketch extruded to the desired length. The material properties of the parametric study specimens were altered to be more representative of average structural steel rather than the specific steel used in the experiments. The yield strength and ultimate strength were set to 55 and 75 ksi respectively while all other material properties were kept the same. The effects of strain hardening and variation in the yield plateau were not investigated because of their minimal effect and rare use in other design applications (Menkulasi et al 2019). Initial imperfection is also difficult to measure and control in design, and therefore was not considered as a parameter in the investigation. Instead, all analyses incorporated imperfection levels equal to the average of what was measured on the experimental specimens. This magnitude was normalized by the thickness of the web and equal to $0.13t_w$ as shown in Table 3.2. A python script was developed to accomplish this repeated process and generate input files for all 120 analyses.

6.2 Analysis Results

The analysis results returned the critical elastic buckling load and ultimate buckling strength for all investigated cases. The data was compiled in Table 6.2 and is organized by beam size, loaded width, and angle of applied load.

Table 6.2: Numerical Parametric Study Results

Analysis	Section	*w/d*	*w*	θ	Ultimate Strength	Elastic Buckling Load
#	Name		in	deg	kips	kips
1	W24X84	0.5	12.05	0	441.1	694.2
2	W24X84	1.0	24.10	0	573.8	869.9
3	W24X84	1.5	36.15	0	758.3	1104.2
4	W24X84	2.0	48.20	0	957.5	1362.9
5	W24X84	2.5	60.25	0	1162.5	1634.1
6	W24X84	0.5	12.05	30	482.3	852.1
7	W24X84	1.0	24.10	30	597.0	1037.3
8	W24X84	1.5	36.15	30	787.6	1300.1
9	W24X84	2.0	48.20	30	1004.9	1598.7
10	W24X84	2.5	60.25	30	1230.3	1915.4
11	W24X84	0.5	12.05	45	572.1	1074.6
12	W24X84	1.0	24.10	45	603.8	1231.1
13	W24X84	1.5	36.15	45	779.1	1517.3
14	W24X84	2.0	48.20	45	1003.6	1876.4
15	W24X84	2.5	60.25	45	1243.3	2271.3
16	W18x60	0.5	9.10	0	322.7	610.7
17	W18x60	1.0	18.20	0	422.1	763.6
18	W18x60	1.5	27.30	0	559.3	968.0
19	W18x60	2.0	36.40	0	708.7	1193.6
20	W18x60	2.5	45.50	0	862.3	1430.2
21	W18x60	0.5	9.10	30	344.1	750.5
22	W18x60	1.0	18.20	30	426.0	909.6
23	W18x60	1.5	27.30	30	562.7	1137.9
24	W18x60	2.0	36.40	30	719.2	1397.8
25	W18x60	2.5	45.50	30	881.4	1673.9
26	W18x60	0.5	9.10	45	405.5	950.2
27	W18x60	1.0	18.20	45	423.2	1082.6
28	W18x60	1.5	27.30	45	549.0	1327.8
29	W18x60	2.0	36.40	45	705.8	1638.1
30	W18x60	2.5	45.50	45	871.5	1981.2

Table 6.2: Numerical Parametric Study Results - Continued

Analysis	Section	*w/d*	*w*	*θ*	Ultimate Strength	Elastic Buckling Load
#	Name		in	deg	kips	kips
31	W18x40	0.5	8.95	0	195.9	267.5
32	W18x40	1.0	17.90	0	252.6	334.6
33	W18x40	1.5	26.85	0	331.7	424.1
34	W18x40	2.0	35.80	0	417.3	522.9
35	W18x40	2.5	44.75	0	504.9	626.7
36	W18x40	0.5	8.95	30	220.0	326.4
37	W18x40	1.0	17.90	30	270.1	398.1
38	W18x40	1.5	26.85	30	352.8	498.8
39	W18x40	2.0	35.80	30	448.7	612.9
40	W18x40	2.5	44.75	30	548.9	734.1
41	W18x40	0.5	8.95	45	262.2	407.7
42	W18x40	1.0	17.90	45	282.5	470.7
43	W18x40	1.5	26.85	45	359.2	581.2
44	W18x40	2.0	35.80	45	459.8	718.6
45	W18x40	2.5	44.75	45	570.9	869.5
46	W16x26	0.5	7.85	0	122.5	144.0
47	W16x26	1.0	15.70	0	156.1	187.2
48	W16x26	1.5	23.55	0	204.2	237.4
49	W16x26	2.0	31.40	0	255.6	292.9
50	W16x26	2.5	39.25	0	308.2	351.2
51	W16x26	0.5	7.85	30	139.6	178.7
52	W16x26	1.0	15.70	30	169.6	221.3
53	W16x26	1.5	23.55	30	220.8	278.8
54	W16x26	2.0	31.40	30	279.7	343.2
55	W16x26	2.5	39.25	30	340.9	411.5
56	W16x26	0.5	7.85	45	167.3	217.3
57	W16x26	1.0	15.70	45	184.7	257.9
58	W16x26	1.5	23.55	45	230.7	232.4
59	W16x26	2.0	31.40	45	295.0	402.3
60	W16x26	2.5	39.25	45	365.9	487.8

Some observations can be made by examining the previous tables. Intuitively, increasing the loaded width *w* results in higher total buckling loads. Additionally, the heavier specimens had the greatest difference between the elastic buckling capacity and ultimate load from the analysis, suggesting that inelastic buckling governed the strength of these specimens. The prediction method discussed in the following chapter contains inelastic considerations when predicting the ultimate buckling strength.

7. PROPOSED PREDICTION METHOD

7.1 Comparison to Existing AISC Recommendations

The current AISC 360-16 web compression buckling equation can be found in Chapter J.10 as Equation J10-8. This equation was first discussed in Chapter 1 and repeated here for convenience.

$$R_n = \frac{24 * t_w^3 \sqrt{E * f_y}}{h} * Q_f \tag{1.1}$$

This equation was developed to predict the behavior of wide flanged sections subjected to concentrated point forces in the case of a beam-to-column moment connection. The AISC commentary suggests the web should be designed as a compression member according to Chapter E when the loaded width is not small compared to the depth of the section. For the purposes of this comparison, any loaded width that was greater than or equal to the section depth was considered "not small." When considering the boundary conditions of the equivalent column, the flanges were assumed to create a fixed-fixed condition. The analysis results were compared with this calculation and presented in a 1-to-1 plot below.

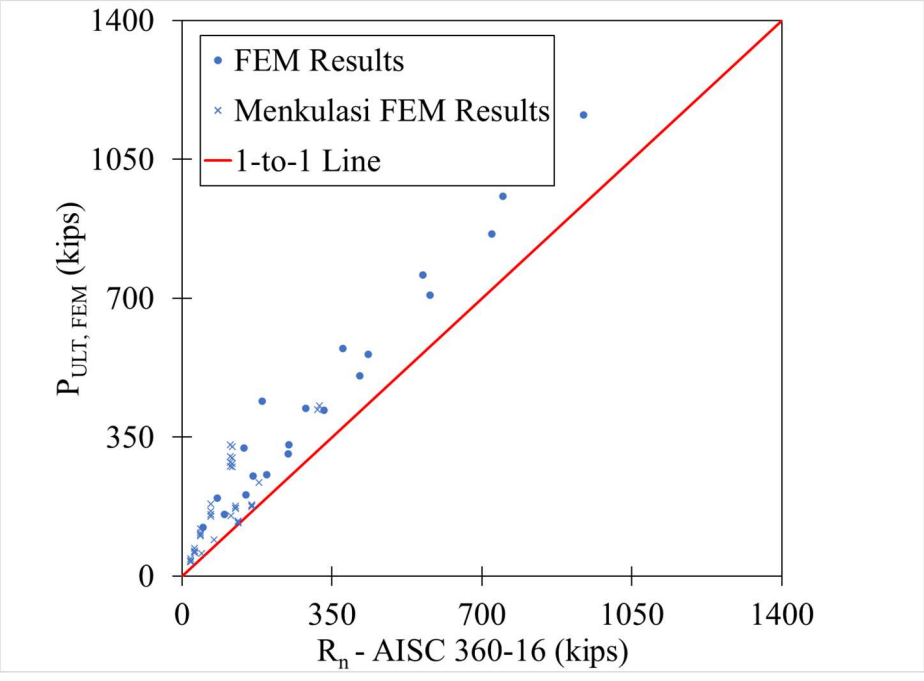

Figure 7.1: 1-to-1 Comparison Plot of the Numerical Data to Existing AISC Provisions

Most of the numerical data points plot above the 1-to-1 line, meaning they are conservative. For smaller buckling strengths with smaller loaded widths, the AISC suggested method does a better job than for larger loaded widths. Overall, the suggested analysis method is a good, conservative approximation. The prediction could be improved by following the procedure in Section 7.5. The AISC equations do not consider the angle of load application as a parameter, so those data points are not used in the comparison.

7.2 Defining the Problem

Classical solutions were combined with semiempirical methods to develop a closed-form prediction method for web compression buckling. In this development, data from the parametric study in this paper was used in conjunction with data obtained by Menkulasi & Farzana (2019) The results obtained by Menkulasi & Farzana are provided in the Appendix. The webs subjected to the load can be treated as a rectangular plate with dimensions a, b, and t_w. The height of the plate, a, is the unstiffened height of the web, h, defined as the clear distance between the flanges minus the fillet or corner radius. The width of the effective plate, b, is defined by the width of the applied load, w, plus a contribution from the load spreading through the depth of the member. A diagram showing these definitions is provided below in Figure 7.2.

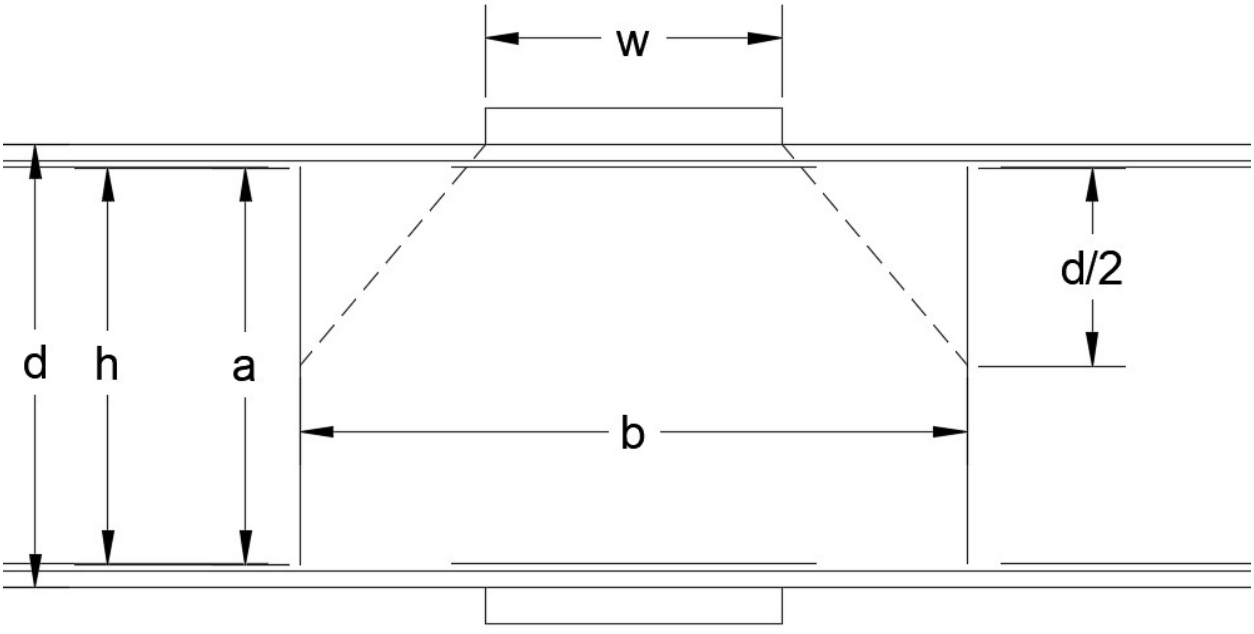

Figure 7.2: Diagram of Assumed Rectangular Plate

The dashed lines represent the spreading of the load from the application region to the midpoint of the web. The horizontal dimension between the intersections is the width of the assumed plate. This spread angle was determined by examining the stress contours of the finite element models when the load was at or near the maximum. The average width between the ends of the compressive stress bulb was the width over which the assumed plate would buckle. An example of the assumed width is shown in Figure 7.3. A spread angle, α, was then calculated to fit this data resulting in an angle of 40 degrees. Figure 7.4 shows how the spread angle is used to determine *b*.

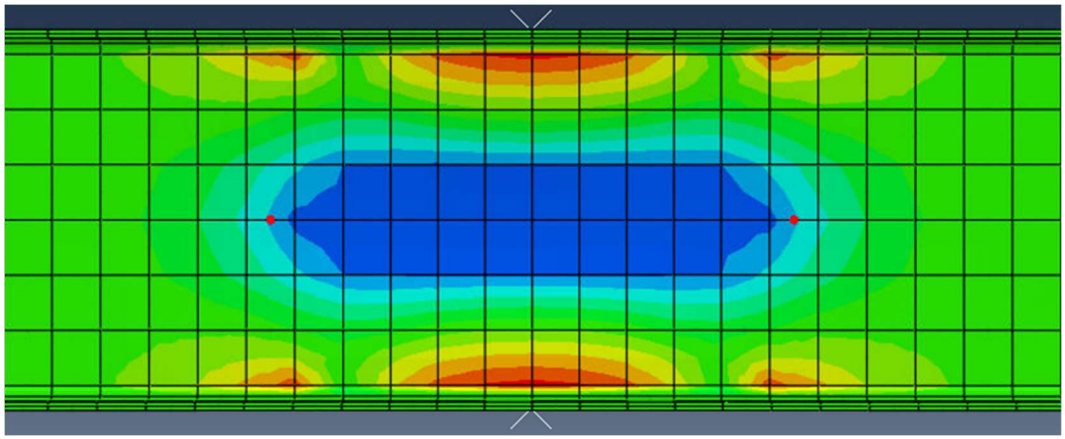

Figure 7.3: Stress Contour Plot from ABAQUS Finite Element Analysis

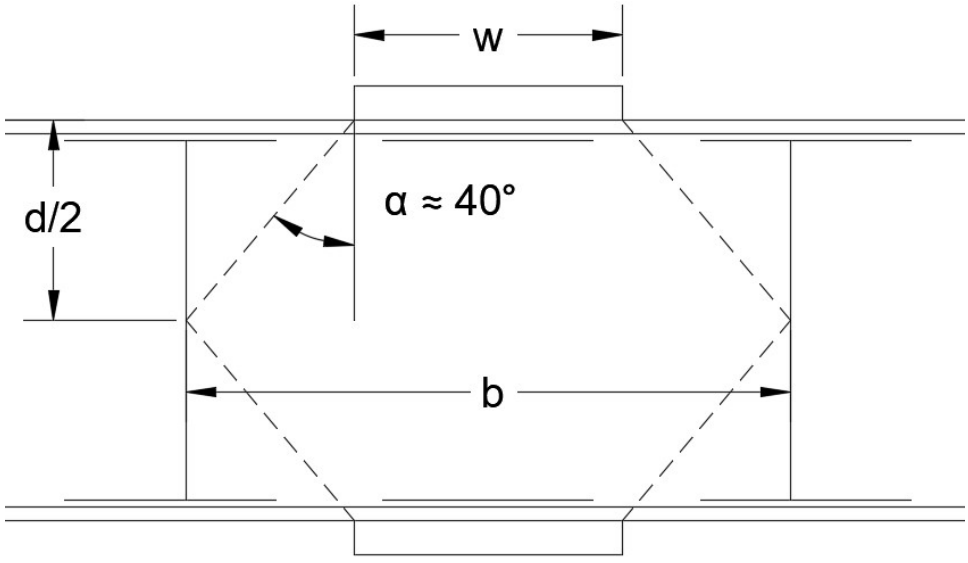

Figure 7.4: Diagram of Spread Angle Relative to Assumed Plate

The results from this geometry are provided in the following equations. The tangent of 40 degrees is approximated as 0.8 for simplicity.

$$a = h = d - 2k = \frac{h}{t_w} * t_w \tag{7.1}$$

$$b = w + 0.8d \tag{7.2}$$

7.3 Determining the Critical Elastic Buckling Load

The elastic buckling load is determined by solving the 4th order differential equation in both orthogonal directions associated with the plate. Many published solutions exist for various edge boundary conditions. Timoshenko and Gere (1963) summarize many of these solutions.

According to Timoshenko, for rectangular, isotropic plates, the overall elastic buckling load, P_{cr}, is described by the following equation:

$$P_{cr} = k * \frac{\pi^2 E t_w^3}{12(1 - v^2) * b} \tag{7.3}$$

P_{cr} in this equation is in units of force, meaning the distributed force is multiplied by the length of loading, w, to give P_{cr}. E and v are the elastic modulus (29000 ksi) and Poisson's Ratio (0.3) respectively, and the buckling factor, k, is a function of the aspect ratio of the plate. Timoshenko provides a function for k when all plate edges are simply supported (SS).

$$k_{SS} = \left(\frac{b}{a} + \frac{a}{b}\right)^2 \tag{7.4}$$

However, when dealing with webs of rolled beams, the plate edges are not simply supported. The loaded edges of the plate are connected to the flanges, which provide rotational restraint to the edge. Therefore, these edges should be analyzed as fixed, or clamped. The unloaded edges are neither pinned, clamped, nor free. They are continuous with the rest of the specimen, which makes classifying a boundary condition very challenging. In defining the width, b, measurements were taken based on points of low stress. Simply supported edges have zero stress along that edge, so reason suggested that these unloaded edges could be approximated as simply supported. As for the loaded edges, the k-function for simply supported case could be modified by a factor to produce a function that could model the fixed condition along the loaded edges. This

assumption is similar to a fixed-fixed column having an effective length of one half of a pin-ended column. Thus, the following equation for k was determined for plates with loaded edges clamped.

$$k = \left(1.67\frac{b}{a} + 0.6\frac{a}{b}\right)^2 \tag{7.5}$$

The two relationships for k were compared with the eigenvalue buckling analysis results from the parametric study. Equivalent values for k were obtained from the finite element results by back calculating from a known P_{cr}. The second, modified equation best captured the behavior observed in the finite element models and is shown in Figure 7.5.

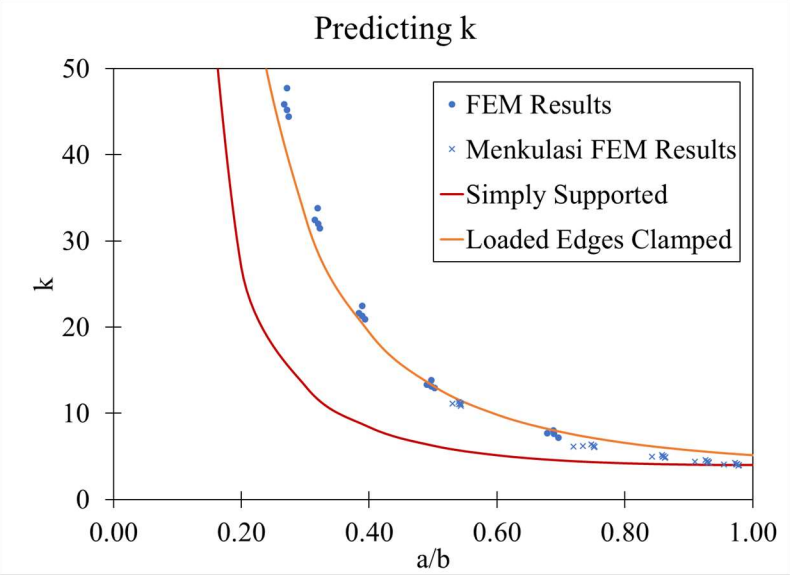

Figure 7.5: Plot of Numerical Results Compared with the Critical Elastic Buckling Load Equations

The orange line representing Equation 7.5, best models the numerical data. The finite element results obtained from the study conducted by Menkulasi & Farzana (2019) are consistently overpredicted. This error comes from differences in the modeling technique employed by the researchers. Menkulasi & Farzana's models used shell elements which do not directly model the fillet region which can contribute to the elastic buckling load.

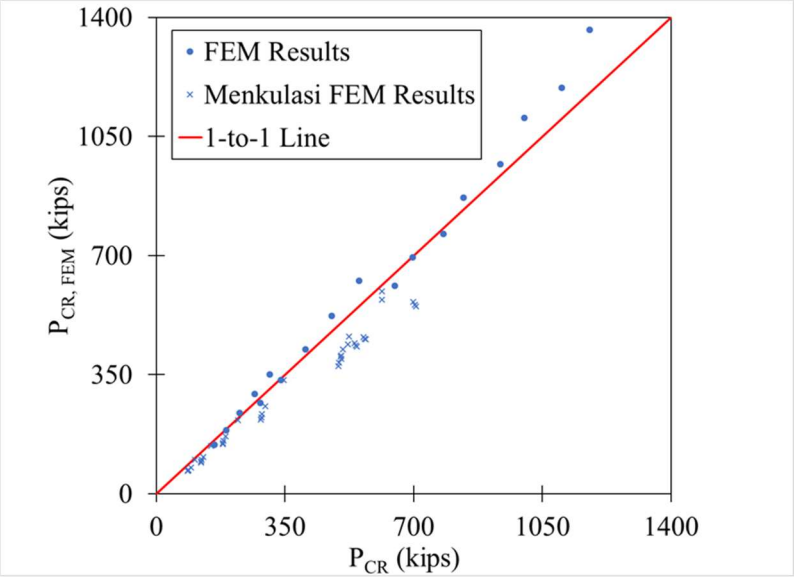

Figure 7.6: 1-to-1 Comparison Plot of the Critical Elastic Load Equation

The comparison between analysis data and the prediction method can also be shown on a 1-to-1 chart. The vertical axis in Figure 7.6 is the analysis results and the horizontal axis is the predicted elastic buckling load calculated from the equation for P_{cr}. The proposed equation captures the analysis results well, as most of the data points fall very close to the 1-to-1 line. Data points from the analyses conducted by Menkulasi & Farzana (2019) unconservatively fall below the line due to the reasons discussed earlier in this section. For specimens that have large critical buckling loads, the equation predicts them conservatively.

7.4 Derivation of Buckling Strength Equation

Due to the compactness of webs in rolled shapes, web compression buckling is largely inelastic. Previous models describing the inelastic buckling of plates comes from research conducted by von Kármán et al (1932). von Kármán showed that as the plate buckles, stresses in the plate redistribute toward the edges, as the edges are the stiffest area in the plate. He then developed an equation for the "effective width," which is the portion of the plate carrying most of the stress at buckling. This effective width is different than the width of the effective plate in the web. If similar behavior was observed in the webs of the numerical models, then Kármán's conclusions could be reasonably applied to this scenario.

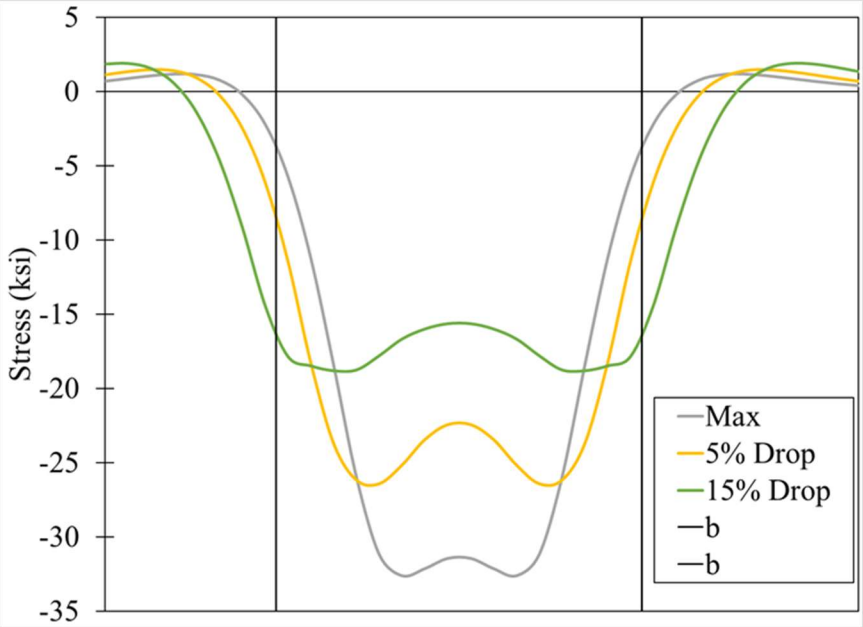

Figure 7.7: Plot of the Average Membrane Stress in Web at Various Load Levels

The Figure 7.7 shows the average membrane stress at the mid-height of the web. The vertical black lines represent the width of the effective plate, b. At the onset and after buckling, the average membrane stress redistributes away from the center of the effective plate and towards the edges. This redistribution of stress is the type of behavior von Kármán described, so relationships derived from his calculation of effective width should also be valid in the case of web compression buckling.

von Kármán developed the following equation to describe the effective width, or the portion of the plate that would carry the most stress at buckling.

$$\frac{b_e}{b} = \sqrt{\frac{\sigma_c}{\sigma_e}}\left(1.0 - 0.22\sqrt{\frac{\sigma_c}{\sigma_e}}\right) \tag{7.6}$$

The term, σ_c is the elastic buckling load and σ_e is the edge stress. The factor of 0.22 in the parentheses is a constant use to calibrate the equation to fit a set of experimental data. This equation can be algebraically modified to represent the average membrane stress divided by the yield stress. Kalyanaraman et al (1977) made this modification to present the following equation.

$$\frac{\sigma_{av}}{\sigma_y} = 1.19\sqrt{\frac{\sigma_c}{\sigma_y}}\left(1.0 - 0.3\sqrt{\frac{\sigma_c}{\sigma_y}}\right) = \frac{P_{ult}}{P_y} \tag{7.7}$$

In this equation, 1.19 and 0.3 are constants used to fit the equation to a set of experimental data. This equation was calibrated for use in thin walled, cold formed steel members, but because it is derived from Kármán's equation for effective width, it was hypothesized that this equation could be used to represent web compression buckling by changing the constants to fit the numerical results. A slenderness parameter, λ, was defined as:

$$\lambda = \sqrt{\frac{\sigma_y}{\sigma_c}} = \sqrt{\frac{P_y}{P_{cr}}} \tag{7.8}$$

$$P_y = b * t_w * f_y \tag{7.9}$$

Substituting the definitions from Equations 7.8 and 7.9 into Kalyanaraman's Equation 7.7 and changing the constants to *A* and *B*, results in an equation describing the available strength in web compression buckling, R_n:

$$\frac{R_n}{P_y} = \frac{A}{\lambda}\left(1.0 - \frac{B}{\lambda}\right) \leq 1.0 \tag{7.10}$$

The upper limit of 1.0 is enforced because the buckling load cannot be greater than the plastic capacity of the web. The constants *A* and *B* were calibrated to the mean of the numerical data, meaning that the average ratio of P/R_n is equal to 1.0. To achieve this result, *A* was set to 0.6 and *B* was set to 0.05. The numerical FEM results are compared to this equation in Figure 7.8 and Figure 7.9.

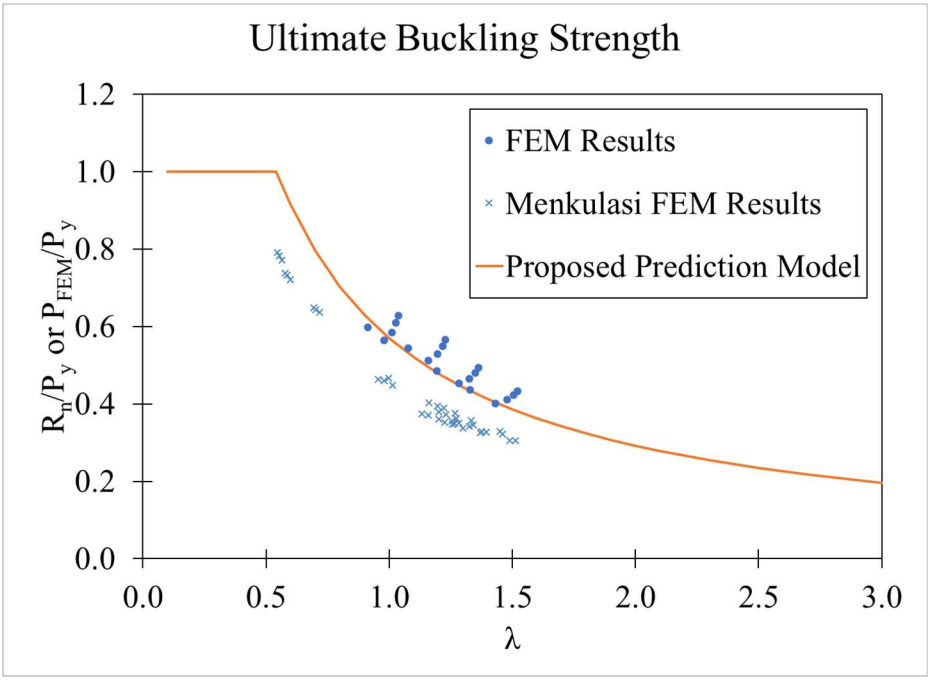

Figure 7.8: Ultimate Buckling Strength Plot for Vertical Load Cases

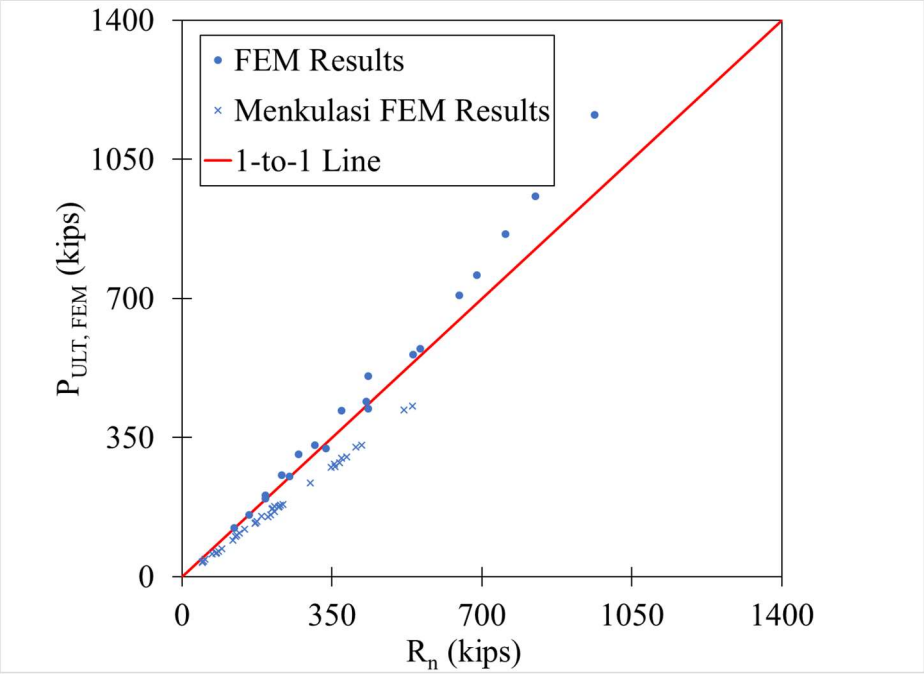

Figure 7.9: 1-to-1 Comparison Plot of the Ultimate Buckling Strength Equation

As shown in the Figure 7.8, the numerical data follow the shape of the curve well, showing strong correlation. Like the critical elastic strength plots, higher capacities are predicted more

conservatively. The data obtained from Menkulasi & Farzana plots below the curve again for ultimate strength similar to the elastic buckling strength plots. Some of the error might have been carried over from the elastic buckling load calculation, but much of the error can be attributed to the levels of imperfection assumed in the numerical models. As mentioned previously, the parametric study conducted for this paper assumed an initial imperfection magnitude of $0.13*t_w$ applied to the first buckling mode shape. Menkulasi & Farzana (2019) applied imperfections of *d/100* to the first mode shape, where *d* is the overall depth of the specimen. On average, *d/100* is 300% larger than $0.13*t_w$, resulting in lower ultimate buckling strengths.

7.5 Examining Web Compression Buckling for Angled Load Cases

The numerical parametric study also investigated the effect of changing the angle of load application, θ. This case is different than changing other parameters because the geometry and physics of the problem change. The best way to treat this system is to treat it like an oblique plate with dimensions *a* and *b* shown in Figure 7.10.

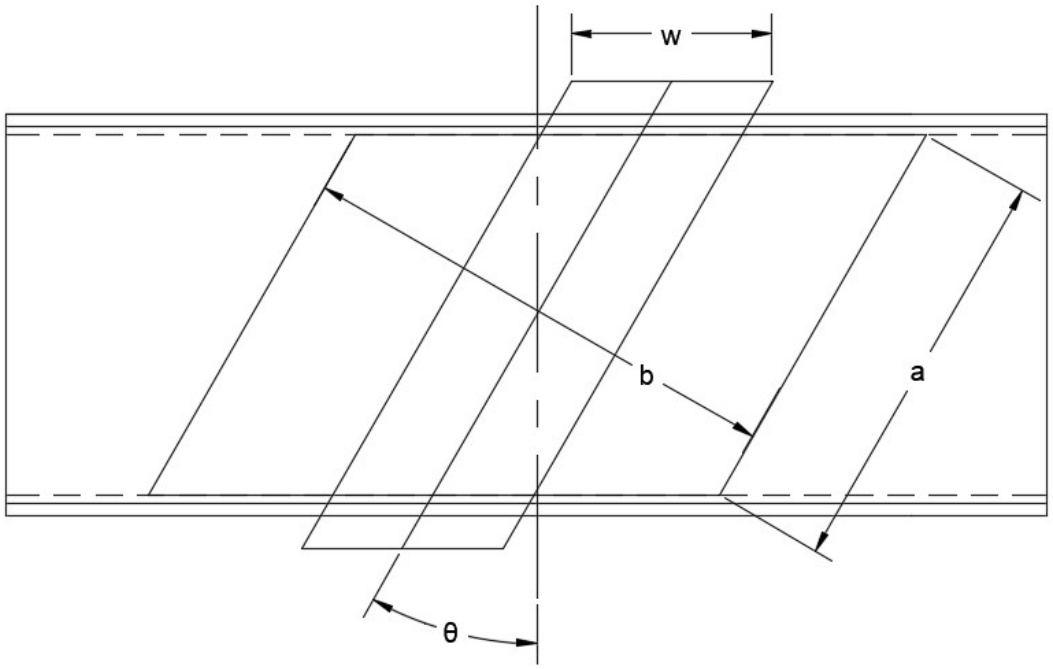

Figure 7.10: Oblique Web Plate Diagram

According to Figure 7.10, the dimensions *a* and *b* can be calculated with the following equations.

$$a = \frac{h}{\cos\theta} \tag{7.11}$$

$$b = w\cos\theta + \frac{0.8d}{\cos\theta} \tag{7.12}$$

When θ is zero, these equations for the plate dimensions become the same as for the vertical cases, keeping compatibility within the models.

7.5.1 Determining the critical elastic buckling load

Yoshimura et al (1963) authored a paper in which they provide classical solutions regarding the elastic buckling load of oblique plates, similar to how the web compression buckling has been defined. This analysis is discussed in greater detail in Section 2.2.2. According to their results, the coefficient k is a function of the aspect ratio of the plate, the cosine of the angle of application, and a third function φ_{cr}. This φ_{cr} is calculated from an eigenvalue solution of a matrix based on the geometric configurations of the plate. When θ is set to zero, the vertical case, φ_{cr} and k are equal to 4, the convergence value for k as a/b increases. This relationship proposed by Yoshimura (1963) could be applied to web compression bucking by making a slight modification, shown in the following equations.

$$k = \frac{k_0}{\cos^3\theta} \tag{7.13}$$

$$k_0 = \left(1.67\frac{b}{a} + 0.6\frac{a}{b}\right)^2 \tag{7.14}$$

Equation 7.13 uses the existing equation for k provided earlier in Equation 7.5 with a modification consistent with the solutions from Yoshimura. The calculated values for k obtained from these equations are then used in the formula for P_{cr} defined previously in Equation 7.1. The numerical results from the parametric study were compared to this relationship and provided in Figure 7.11.

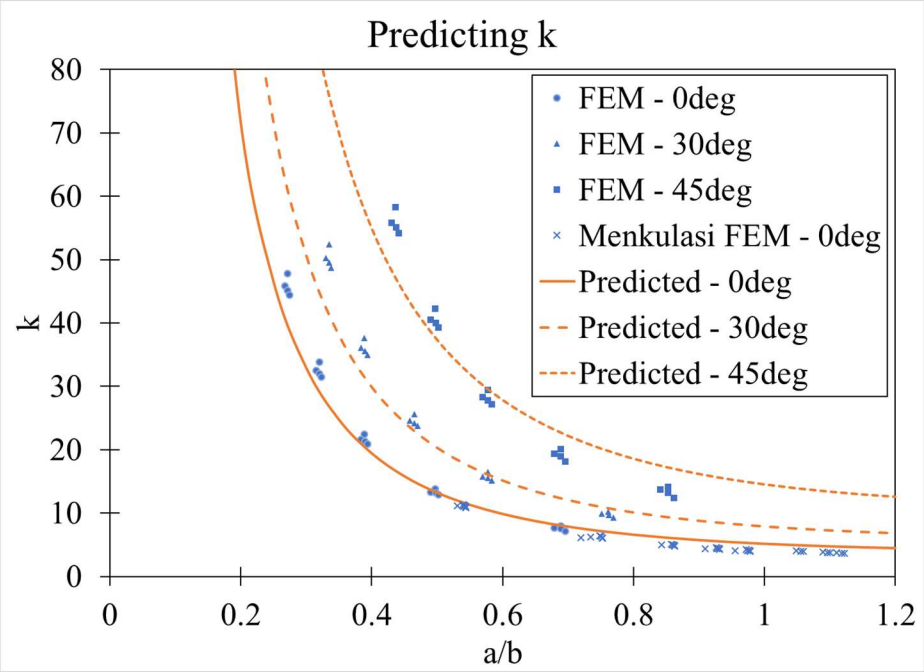

Figure 7.11: Plot of Numerical Results Compared with the Critical Elastic Buckling Load Equations for Angled Load Cases

As shown in Figure 7.11, the data follows the proposed relationship well. The greatest error occurs when θ is 45 degrees. This error is an overprediction for large aspect ratios and an underprediction for small aspect ratios. The geometry of the problem could be changing when θ is large due to geometric limits, so more investigation was done in an attempt to better understand the problem and the sources of the error in Section 7.5.2.

7.5.2 Possible limitations on the width, *b*

The dimension b is measured along an axis orthogonal to the direction of the load, and in theory the calculated value of b could exceed what is physically available in the specimen. This notion would suggest that the natural limit on b should be $h/\sin\theta$. To verify this claim, the stress contours of the finite element models were examined before, during, and after buckling in cases where θ equaled 45 degrees. The following figures are from an analysis of a W18X40 beam with w set to 18 inches and θ equal to 45 degrees. This specimen provides a clear example of the common pattern observed in all cases.

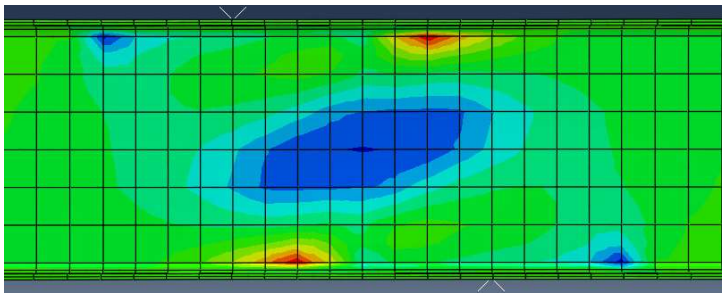

(a)

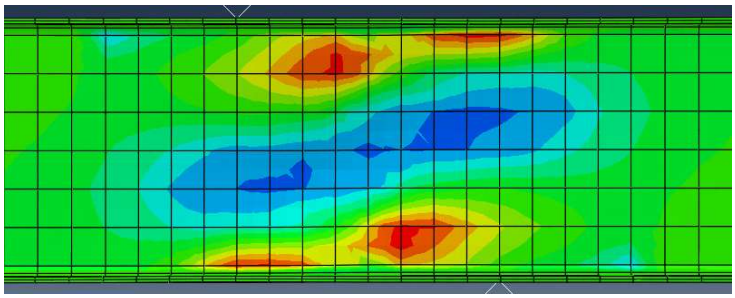

(b)

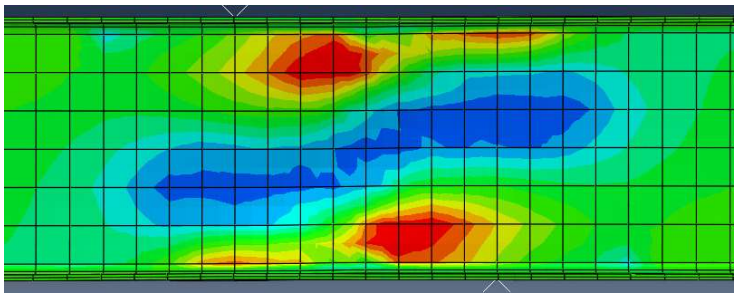

(c)

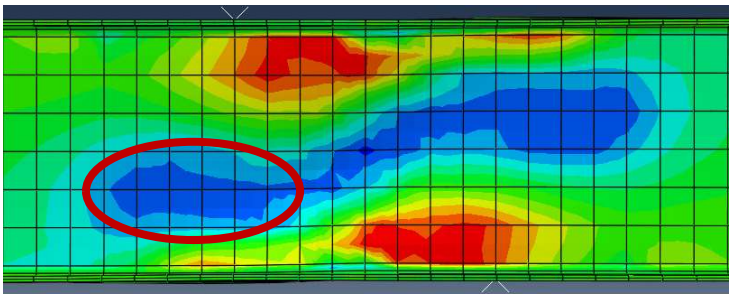

(d)

Figure 7.12: Stress Contour Progression Plots from (a) Before Maximum Load to (b) at the Maximum Load to (c) when the Load Decreases to 90% of the Maximum to (d) when the Load Decreases to 75% of the Maximum

In Figure 7.12(a)-(d), the blue regions are areas of high compressive stress, orange and red are areas of high tension stress, and green areas have small magnitudes of stress. The stresses plotted in the contours are the vertical components of stress, S22 as defined in the model. Figure 7.12(a) is taken before the maximum load is reached, (b) is taken immediately after the maximum load but before much of the deformations, and (c) and (d) are captured after buckling has occurred. The horizontal "tails" of compressive stress marked by the red ellipse in (d) suggest that although the definition of *b* reaches the geometric limit, the stress does not simply stop progressing away from the applied center. Another observation can be made by drawing an imaginary line through the center of the contours in (a), then comparing that to the line of applied load. This drawing is shown in Figure 7.13.

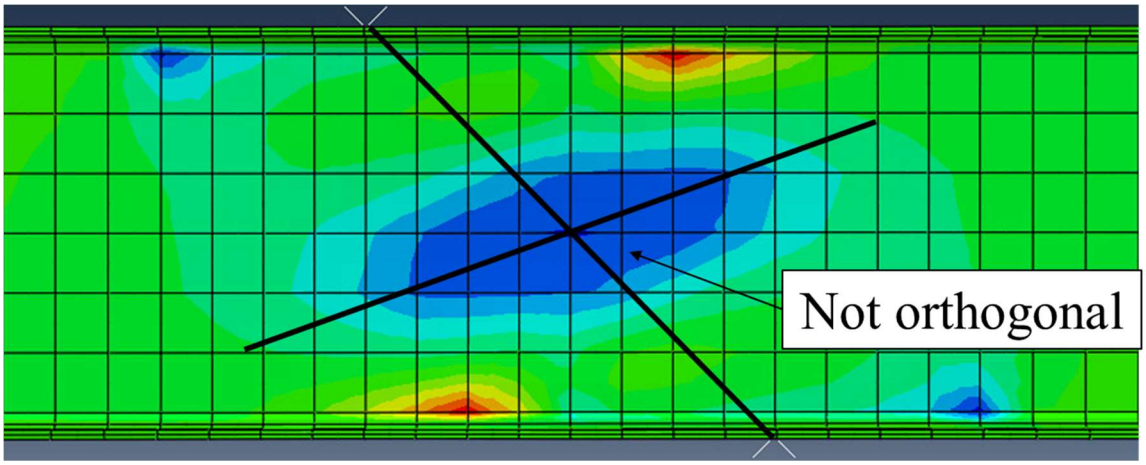

Figure 7.13: Plot of the Non-Orthogonality of Stress Contours Seen in Figure 7.12(a)

The line through the center of the stress contour is not orthogonal to the direction of the loading like the assumption in the oblique plate buckling solution. This observation combined with the carryover trails identified in the circle on Figure 7.12(d) creates a great deal of complexity in this problem once the angle of application gets larger than 30 degrees. Equation 7.13 proposed in 7.5.1 and plotted in Figure 7.11 does a fairly good job at predicting the results without considering these abnormalities. Therefore, the provided relationships can be used as a simple approximation, but if a more detailed solution is desired the effects discussed in this section should be addressed.

7.5.3 Ultimate buckling strength of angled load cases

Since the angled load effects are mostly contained in the calculation of elastic buckling load, the existing ultimate strength equation (7.10) from Section 7.3 should still be applicable to these cases. A plot of the numerical data for all cases is compared with the proposed equation and shown below in Figure 7.14.

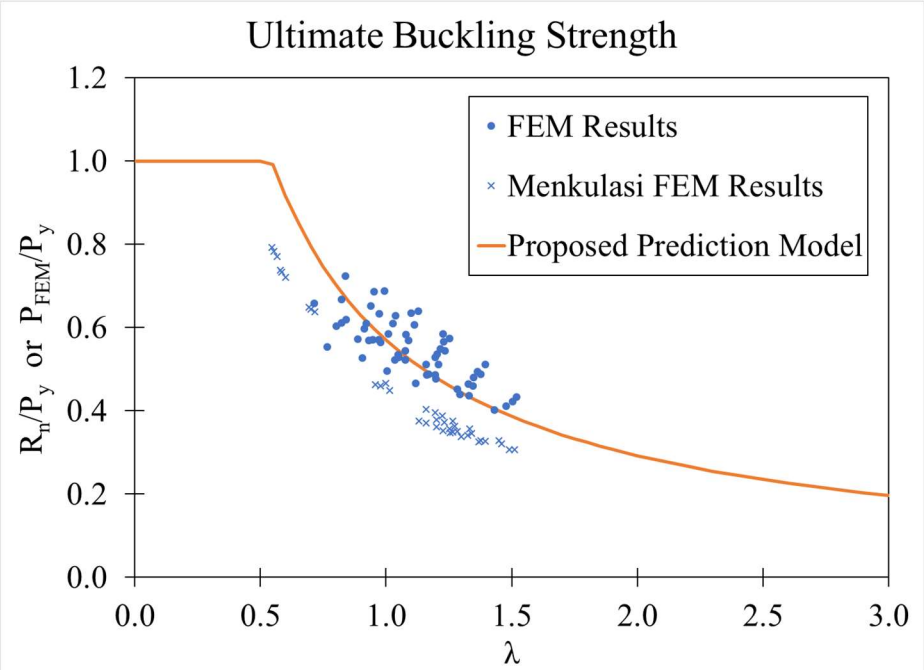

Figure 7.14: Ultimate Buckling Strength Plot for All Load Cases

The data points are slightly more scattered with the addition of the angled load cases, but this scatter is likely due to the errors discussed earlier in Section 7.5.2. The constants *A* and *B* are 0.6 and 0.05 respectively, just like the vertical cases.

7.6 Summary of Proposed Calculation Method

The steps in the calculation go as follows.

First, the dimensions of the effective plate are defined according to the following equations.

$$a = \frac{h}{\cos\theta} \tag{7.15}$$

$$b = w\cos\theta + \frac{0.8d}{\cos\theta} \tag{7.16}$$

The yield load of the plate is then calculated.

$$P_y = b * t_w * f_y \tag{7.17}$$

Then, the elastic buckling factor, k is calculated.

$$k = \frac{k_0}{\cos^3 \theta} \tag{7.18}$$

$$k_0 = \left(1.67\frac{b}{a} + 0.6\frac{a}{b}\right)^2 \tag{7.19}$$

The value obtained for k is then used to solve for the critical elastic buckling load, P_{cr}.

$$P_{cr} = k * \frac{\pi^2 E t_w^3}{12(1-v^2) * b} \tag{7.20}$$

Once the elastic buckling load is calculated, the slenderness parameter, λ, can be calculated.

$$\lambda = \sqrt{\frac{P_y}{P_{cr}}} \tag{7.21}$$

The slenderness parameter is then the independent variable used in the ultimate buckling strength equation, where R_n is the nominal available strength in web compression buckling.

$$\frac{R_n}{P_y} = \frac{0.6}{\lambda}\left(1.0 - \frac{0.05}{\lambda}\right) \leq 1.0 \tag{7.22}$$

7.7 Assumptions and Limitations of Proposed Method

7.7.1 Assumptions in the prediction method

Imperfection levels used in the numerical models

According to Figure 7.8 and Figure 7.14, the amount of out of plane imperfection applied to the finite element models greatly impacts the final strength. For the models generated in the parametric study discussed in Chapter 6, imperfections of magnitude 0.13*t_w were applied to the

models. This magnitude was chosen after examining the results of the measurements conducted in Section 3.5. As discussed in that section, measurements were only taken from one heat of W18X40 beams from one manufacturer. This assumed level of imperfection may only be valid for this size of beam from this manufacturer. This assumption could be validated by a more comprehensive study of out-of-plane imperfections in steel wide flange member webs. If the assumed levels of imperfection used in the analyses in Chapter 6 are not representative of the comprehensive average, the calibration constants in Equation 7.22 should be adjusted.

Consideration of residual stresses

Residual stresses were not considered in the parametric study. Residual stresses in hot rolled wide flange shapes are typically a result of differential cooling, and thus these stresses primarily act along the longitudinal axis of the beam. However, there can be cases where significant residual stresses can be found in the perpendicular direction, the direction of stress associated with web compression buckling. These stresses would increase in significance as the section depth increases.

Consideration of orthotropic material properties

The material properties used in all numerical models were the result of tension coupons cut in the longitudinal direction of the beam. Like when discussing residual stresses, the yield strength, yield plateau, and ultimate strength of the steel could have different properties when measured in the orthogonal direction. However, for this analysis and prediction method structural steel was considered an isotropic material having identical properties in all directions.

7.7.2 Applicability limitations of the prediction method

Limitations regarding loading width

The loaded widths investigated in Chapter 6 ranged from 0.5 to 2.5 times the depth of the section. The results obtained by Menkulasi & Farzana (2019) considered loaded widths down to 0.05 times the section depth. Considering the results shown in Figure 7.1, the current AISC Equation J10-8 (Equation 1.1) is applicable for loaded widths less than 0.5 times the section depth. For loaded widths between 0.5 and 2.5 times the section depth, the prediction method summarized

in Section 7.6 should be used. When the loaded width exceeds 2.5 times the section depth, the proposed prediction method becomes more conservative, as shown in Figure 7.9. Additionally, the equivalent column approach recommended by the AISC Chapter J Commentary becomes less conservative and more accurately predicts the result. Therefore, as the loaded width exceeds 2.5 times the section depth, both methods could be used with similar degrees of accuracy.

Limitations on angle of application

As discussed in Section 7.5.2, the proposed prediction method yields results with increasing errors as the angle of application increases past 30°. Possible sources of this error are also discussed in Section 7.5.2. These errors are considered negligible for the ease of calculation in the prediction method, but it is advised that supplementary analyses be used in conjunction with the proposed method when the angle of application is greater than 30°.

Limitations regarding member size

The parametric study discussed in Chapter 6 considered 4 beam specimens ranging from depths of 16 to 24 inches with various web slenderness ratios shown in Table 6.1. The sections were chosen to provide data for common beam depths and sizes but may not accurately represent the behavior of beam sections with properties outside this range. Sections considered slender in compression and webs considered slender in shear could behave differently than compact sections and elements. Additionally, sections and webs designated as “heavy” could also exhibit slightly different behavior.

Limitations regarding the applied load

All cases analyzed in Chapter 6 featured uniform compressive forces on the top and bottom flanges. The prediction for the critical elastic buckling load in web compression buckling (Equations 7.3, 7.5, 7.18, 7.19) are based on classical plate buckling solutions with uniform compression loads. Therefore, the prediction methods do not apply to cases with varying distributed loads across the loaded width.

8. CONCLUSIONS

The current design equation in AISC 360-16 does not account for the loaded width as a parameter in the calculation of web compression buckling strength. Through a series of experimental tests and numerical simulations, this parameter proved to play a critical role in predicting the ultimate buckling strength. The experimental tests also confirm that no time dependent effects associated with creep are present in the case of web compression buckling.

In lieu of providing a way to incorporate loaded width into Equation J10-8, AISC 360 suggests analyzing those cases as columns according to the provisions of Chapter E. This method was found to be an adequate, but conservative estimation of the overall strength of this limit state.

The method proposed in this paper analyzes the web as a rectangular plate with dimensions defined in Chapter 7. Using this assumed plate, the elastic buckling load and ultimate buckling load are calculated according to the provisions summarized in Section 7.5. This method more accurately predicts the behavior of web compression buckling than the current design recommendations.

APPENDIX

The following tables are results from the study conducted by Menkulasi & Farzana (2019) referenced in Section 7.

Table 8.1: Critical Elastic Buckling Loads from Menkulasi & Farzana (2019)

Table 7
Comparison of predicted and computed elastic buckling loads (kN).

Section	h/w	Interior Loading					End Loading		
		Lagerqvist Johannsson [7] (P_{crl_LJ})	Proposed ($P_{crl\ proposed}$)	FEA ($P_{crl\ FEA}$)	Ratio = $P_{crl\text{-}FEA}/P_{crl\text{-}predicted}$		Proposed ($P_{crl\ proposed}$)	FEA ($P_{crl\ FEA}$)	$P_{crl\ FEA}/P_{crl\ proposed}$
					$P_{crlFEA}/P_{crl\ LJ}$	$P_{crl\ FEA}/P_{crl\ proposed}$			
W 200 × 15	1	416	419	446	1.07	1.06	358	353	0.99
W 310 × 23.8		588	594	626	1.06	1.05	506	496	0.98
W 410 × 46.1		879	883	961	1.09	1.09	754	760	1.01
W 530 × 66		1374	1387	1488	1.08	1.07	1181	1184	1.00
W 690 × 125		2431	2449	2649	1.09	1.08	2087	2104	1.01
W 760 × 134		2333	2353	2537	1.09	1.08	2002	2019	1.01
W 200 × 15	2	345	343	344	1.00	1.00	216	213	0.99
W 310 × 23.8		489	487	483	0.99	0.99	305	300	0.98
W 410 × 46.1		729	723	749	1.03	1.04	454	463	1.02
W 530 × 66		1141	1136	1145	1.00	1.01	712	715	1.00
W 690 × 125		2019	2006	2054	1.02	1.02	1257	1277	1.02
W 760 × 134		1939	1929	1956	1.01	1.01	1207	1220	1.01
W 200 × 15	3	322	322	317	0.98	0.99	171	159	0.93
W 310 × 23.8		456	456	441	0.97	0.97	242	237	0.98
W 410 × 46.1		680	677	691	1.02	1.02	360	369	1.03
W 530 × 66		1064	1064	1046	0.98	0.98	565	566	1.00
W 690 × 125		1882	1878	1888	1.00	1.01	997	1014	1.02
W 760 × 134		1807	1806	1791	0.99	0.99	958	967	1.01
W 200 × 15	4	310	312	304	0.98	0.97	150	148	0.99
W 310 × 23.8		439	443	421	0.96	0.95	213	208	0.98
W 410 × 46.1		655	657	664	1.01	1.01	316	326	1.03
W 530 × 66		1025	1034	998	0.97	0.97	496	495	1.00
W 690 × 125		1813	1824	1810	1.00	0.99	876	890	1.02
W 760 × 134		1742	1755	1713	0.98	0.98	841	847	1.01
W 200 × 15	5	303	308	297	0.98	0.96	138	137	0.99
W 310 × 23.8		429	437	410	0.96	0.94	196	191	0.97
W 410 × 46.1		640	648	649	1.01	1.00	291	299	1.03
W 530 × 66		1002	1019	971	0.97	0.95	458	454	0.99
W 690 × 125		1772	1798	1767	1.00	0.98	808	818	1.01
W 760 × 134		1702	1730	1669	0.98	0.96	777	776	1.00
W 250 × 73	10	1904	1980	2050	1.08	1.04		Avg	1.00
W 310 × 97		2357	2454	2510	1.07	1.02		COV	0.02
W 360 × 91		1817	1892	1967	1.08	1.04		Min.	0.93
W 250 × 73	15	1873	1995	2029	1.08	1.02		Max.	1.03
W 310 × 97		2317	2473	2473	1.07	1.00		% cons.	57
W 360 × 91		1787	1907	1940	1.09	1.02			
W 250 × 73	20	1857	2015	2018	1.09	1.00			
W 310 × 97		2298	2499	2450	1.07	0.98			
W 360 × 91		1772	1927	1922	1.08	1.00			
				Avg.	1.03	1.01			
				COV	0.05	0.04			
				Min.	0.96	0.94			
				Max.	1.09	1.09			
				% cons.	59	54			

Table 8.2: Ultimate Buckling Strength from Menkulasi & Farzana (2019)

Table 8
Comparison of predicted and computed web buckling capacities (kN).

Section	$\frac{h}{w}$	Interior Loading									End Loading						
		AISC 360–16 (R_{n_AISC})	Lager. and Johan. [7] (R_{n_LJ})	Prop.1 ($R_{n\_P\_1}$)	Prop.2 ($R_{n\_P\_2}$)	FEA (R_{n_FEA})	Ratio = $R_{n\text{-}FEA}/R_{n\text{-}predicted}$				AISC 360–16 (R_{n_AISC})	Prop.1 ($R_{n\_P\_1}$)	Prop.2 ($R_{n\_P\_2}$)	FEA (R_{n_FEA})	Ratio = $R_{n\text{-}FEA}/R_{n\text{-}predicted}$		
							$\frac{R_{n\_FEA}}{R_{n\_AISC}}$	$\frac{R_{n\_FEA}}{R_{n\_LJ}}$	$\frac{R_{n\_FEA}}{R_{n\_P\_1}}$	$\frac{R_{n\_FEA}}{R_{n\_P\_2}}$					$\frac{R_{n\_FEA}}{R_{n\_AISC}}$	$\frac{R_{n\_FEA}}{R_{n\_P\_1}}$	$\frac{R_{n\_FEA}}{R_{n\_P\_2}}$
W 200 × 15		89	245	291	235	254	2.85	1.04	0.87	1.08	45	237	191	210	4.70	0.89	1.10
W 310 × 23.8		127	410	473	392	411	3.24	1.00	0.87	1.05	63	394	324	340	5.37	0.86	1.05
W 410 × 46.1	1	188	662	741	638	681	3.63	1.03	0.92	1.07	94	613	514	547	5.82	0.89	1.06
W 530 × 66		296	1049	1163	1001	1050	3.55	1.00	0.90	1.05	148	976	828	867	5.86	0.89	1.05
W 690 × 125		522	1830	2042	1747	1868	3.58	1.02	0.91	1.07	261	1703	1432	1496	5.74	0.88	1.05
W 760 × 134		502	1910	2025	1809	1909	3.80	1.00	0.94	1.06	251	1709	1505	1521	6.06	0.89	1.01
W 200 × 15		89	177	202	164	196	2.20	1.11	0.97	1.19	45	129	105	125	2.80	0.97	1.19
W 310 × 23.8		127	293	336	271	316	2.49	1.08	0.94	1.17	63	220	178	205	3.24	0.93	1.15
W 410 × 46.1	2	188	477	549	448	534	2.84	1.12	0.97	1.19	94	346	283	338	3.60	0.98	1.20
W 530 × 66		296	749	849	689	808	2.73	1.08	0.95	1.17	148	554	454	525	3.55	0.95	1.16
W 690 × 125		522	1314	1495	1213	1454	2.79	1.11	0.97	1.20	261	963	786	930	3.57	0.97	1.18
W 760 × 134		502	1363	1508	1240	1472	2.93	1.08	0.98	1.19	251	982	825	951	3.79	0.97	1.15
W 200 × 15		89	154	169	141	178	1.99	1.16	1.05	1.27	45	93	77	90	2.02	0.97	1.17
W 310 × 23.8		127	252	283	229	285	2.25	1.13	1.01	1.24	63	161	130	160	2.53	0.99	1.24
W 410 × 46.1	3	188	414	476	384	489	2.60	1.18	1.03	1.27	94	256	206	262	2.79	1.02	1.27
W 530 × 66		296	645	725	583	729	2.47	1.13	1.01	1.25	148	409	331	409	2.77	1.00	1.24
W 690 × 125		522	1136	1281	1031	1329	2.55	1.17	1.04	1.29	261	710	573	724	2.78	1.02	1.26
W 760 × 134		502	1174	1296	1046	1342	2.67	1.14	1.04	1.28	251	734	599	734	2.93	1.00	1.22
W 200 × 15		89	142	152	129	169	1.89	1.19	1.11	1.31	45	74	63	86	1.93	1.16	1.37
W 310 × 23.8		127	232	255	208	271	2.14	1.17	1.06	1.30	63	130	105	138	2.18	1.06	1.31
W 410 × 46.1	4	188	381	437	351	469	2.50	1.23	1.07	1.33	94	209	168	231	2.46	1.11	1.37
W 530 × 66		296	591	656	529	694	2.35	1.17	1.06	1.31	148	334	269	350	2.37	1.05	1.30
W 690 × 125		522	1045	1164	940	1263	2.42	1.21	1.08	1.34	261	579	466	627	2.40	1.08	1.34
W 760 × 134		502	1077	1176	947	1276	2.54	1.19	1.08	1.35	251	603	487	639	2.55	1.06	1.31
W 200 × 15		89	134	141	121	162	1.81	1.20	1.15	1.33	45	63	54	80	1.79	1.28	1.48
W 310 × 23.8		127	219	237	196	261	2.06	1.19	1.10	1.33	63	111	91	126	1.99	1.14	1.39
W 410 × 46.1	5	188	362	412	332	454	2.42	1.26	1.10	1.37	94	180	145	212	2.26	1.18	1.46
W 530 × 66		296	559	611	497	670	2.27	1.20	1.10	1.35	148	287	232	320	2.16	1.12	1.38
W 690 × 125		522	989	1090	884	1222	2.34	1.24	1.12	1.38	261	497	402	577	2.21	1.16	1.43
W 760 × 134		502	1017	1099	887	1235	2.46	1.21	1.12	1.39	251	521	419	581	2.32	1.12	1.39
W 250 × 73	10	581	620	596	590	618	1.06	1.00	1.04	1.05				Avg.	3.22	1.02	1.24
W 310 × 97		721	786	748	738	804	1.12	1.02	1.08	1.09				COV	0.41	0.10	0.11
W 360 × 91		556	700	737	667	786	1.41	1.12	1.07	1.18				Min.	1.79	0.86	1.01
W 250 × 73	15	581	603	574	579	605	1.04	1.00	1.05	1.05				Max.	6.06	1.28	1.48
W 310 × 97		721	763	718	721	787	1.09	1.03	1.10	1.09				%Con.	100	50	100
W 360 × 91		556	677	707	651	765	1.38	1.13	1.08	1.18							
W 250 × 73	20	581	594	564	574	600	1.03	1.01	1.06	1.04							
W 310 × 97		721	751	703	715	778	1.08	1.04	1.11	1.09							
W 360 × 91		556	666	693	644	756	1.36	1.14	1.09	1.17							
						Avg.	2.28	1.12	1.03	1.21							
						COV	0.34	0.07	0.07	0.10							
						Min.	1.03	1.00	0.87	1.04							
						Max.	3.80	1.26	1.15	1.39							
						% Con.	100	95	69	100							

REFERENCES

AISC Committee. (2010). Specification for structural steel buildings (ANSI/AISC 360-10). *American Institute of Steel Construction, Chicago-Illinois*.

Brnic, J., Canadija, M., Turkalj, G., & Lanc, D. (2010). Structural steel ASTM A709—behavior at uniaxial tests conducted at lowered and elevated temperatures, short-time creep response, and fracture toughness calculation. *Journal of engineering mechanics*, *136*(9), 1083-1089.

Chen, W. F., & Newlin, D. E. (1971). Column web strength in steel beam-to-column connections (ASCE Meeting reprint 1524).

Chen, W. F., & Newlin, D. E. (1973). Column Web Strength in Beam-to-Column Connection. *Journal of the Structural Division*, *99*(9), 1978-1984.

Chen, W. F., & Oppenheim, I. J. (1970). Web buckling strength of beam-to-column connections, September 1970 (74-1) PB 234 621/AS.

Chen, W. F., & Oppenheim, I. J. (1974). Web Buckling Strength of Beam-to-Column Connections. *Journal of the Structural Division*, *100*(1), 279-285.

Kalyanaraman, V., Winter, G., & Pekoz, T. (1977). Unstiffened compression elements. *Journal of the Structural Division*, *103*(9), 1833-1848.

Menkulasi, F., & Farzana, N. (2019). Web compression buckling capacity prediction for unstiffened I-sections with opposite patch loading.*Journal of Constructional Steel Research*,*162*, 105728.

Menkulasi, F., Farzana, N., Moen, C.D., Eatherton, M.R. (2016). "Revisiting Web Compressing Buckling for Wide Flange Sections" *Proceedings of the Annual Stability Conference.* Orlando, FL. April 12-15, 2016.

Sener, K., Witte, J., Varma, A.H. (2019). "On the influence of load width on web compression buckling strength" *Proceedings of the Annual Stability Conference.* St. Louis, MO. April 2-5, 2019.

Timoshenko, S. P., & Gere, J. M. (1963). *Theory of elastic stability*. McGraw-Hill Book Company, Inc.

von Kármán, T., Sechler, E. E., and Donnell, L. H. (1932). Strength of Thin Plates in Compression. *Trans. ASME*, *54*, 53-57.

Winter, G. (1947). Strength of Thin Steel Compression Flanges. *Trans. ASCE*, *112*, 527.

Wittrick, W. H. (1954). Correlation between some stability problems for orthotropic and isotropic plates under bi-axial and uni-axial direct stress. *The Aeronautical Quarterly*, *4*(1), 83-92.

Yoshimura, Y., & Iwata, K. (1963). Buckling of simply supported oblique plates. *Journal of Applied Mechanics*, *30*(3), 363-366.

Ziemian, R. D. (Ed.). (2010). *Guide to stability design criteria for metal structures*. John Wiley & Sons.